OMEGA – OSIRIS Mapping of Emission-line Galaxies in A901/2 – III. Galaxy properties across projected phase space in A901/2

Tim Weinzirl,[1] Alfonso Aragón-Salamanca,[1]* Meghan E. Gray,[1] Steven P. Bamford,[1] Bruno Rodríguez del Pino,[1,2] Ana L. Chies-Santos,[3] Asmus Böhm,[4] Christian Wolf[5] and Richard J. Cool[6,7]

[1]*School of Physics and Astronomy, The University of Nottingham, University Park, Nottingham NG7 2RD, UK*

[2]*Centro de Astrobiología, INTA-CSIC, Torrejón de Ardoz, 28850, Madrid, Spain*

[3]*Departamento de Astronomia, Instituto de Física, Universidade Federal do Rio Grande do Sul, 91501-970 Porto Alegre, RS, Brazil*

[4]*Institute for Astro- and Particle Physics, University of Innsbruck, Technikerstr. 25/8, A-6020 Innsbruck, Austria*

[5]*Research School of Astronomy and Astrophysics, Australian National University, Cotter Road, Weston Creek, ACT 2611, Australia*

[6]*MMT Observatory, Tucson, AZ 85721, USA*

[7]*Netflix, 100 Winchester Circle, Los Gatos, CA 95032, USA*

ABSTRACT

We conduct a comprehensive projected phase-space analysis of the A901/2 multicluster system at $z \sim 0.165$. Aggregating redshifts from spectroscopy, tunable-filter imaging and prism techniques, we assemble a sample of 856 cluster galaxies reaching $10^{8.5}$ $M_{\odot}$ in stellar mass. We look for variations in cluster galaxy properties between virialized and non-virialized regions of projected phase space (PPS). Our main conclusions point to relatively gentle environmental effects, expressed mainly on galaxy gas reservoirs. (1) Stacking the four subclusters in A901/2, we find galaxies in the virialized region are more massive, redder and have marginally higher Sérsic indices, but their half-light radii and Hubble types are not significantly different. (2) After accounting for trends in stellar mass, there is a remaining change in rest-frame colour across PPS. Primarily, the colour difference is due to the absence in the virialized region of galaxies with rest frame $B - V < 0.7$ and moderate-to-high ($M_{\star} > 10^{9.85}$ $M_{\odot}$) stellar mass. (3) There is an infalling population of lower mass ($M_{\star} \leq 10^{9.85}$ $M_{\odot}$), relatively blue ($B - V < 0.7$) elliptical or spheroidal galaxies that are strikingly absent in the virialized region. (4) The number of bona fide star-forming and active galactic nucleus galaxies in the PPS regions is strongly dictated by stellar mass. However, there remains a reduced fraction of star-forming galaxies in the centres of the clusters at fixed stellar mass, consistent with the star formation–density relation in galaxy clusters. (5) There is no change in specific Hα-derived star formation rates of star-forming galaxies at fixed mass across the cluster environment. This suggests that pre-processing of galaxies during infall plays a prominent role in quenching star formation.

Key words: instrumentation: interferometers – galaxies: clusters: individual: A901/2 – galaxies: distances and redshifts – galaxies: star formation.

1 INTRODUCTION

In hierarchical models of galaxy evolution, observable properties of galaxies, such as structure and star formation history, are determined by different mass assembly mechanisms, secular processes and environment. In particular, hierarchical growth proceeds through gas and stars assembled via major (e.g. Toomre 1977; Barnes 1988; Khochfar & Silk 2006, 2009; Hopkins et al. 2009) and minor (e.g. Hopkins et al. 2009; Oser et al. 2012; Hilz, Naab & Ostriker 2013) mergers with other galaxies, as well as gas accretion from the halo and cold streams (e.g. Birnboim & Dekel 2003; Kereš et al. 2005; Dekel & Birnboim 2006; Ocvirk, Pichon & Teyssier 2008). Bar-driven gas inflows can efficiently redistribute angular momentum and mass, and drive internal secular evolution (e.g. Kormendy 1993; Kormendy & Kennicutt 2004; Jogee, Scoville & Kenney 2005). In high-density environments (e.g. rich galaxy clusters), physical processes such as ram-pressure stripping (Gunn & Gott 1972; Fujita &

* E-mail: alfonso.aragon@nottingham.ac.uk

Nagashima 1999), galaxy harassment (Barnes & Hernquist 1991; Moore et al. 1996; Hashimoto et al. 1998; Gnedin 2003) and strangulation (Larson, Tinsley & Caldwell 1980) can alter star formation history and galaxy stellar structure.

Yet, after over a century of exploring galaxies, we are still grappling with questions of how galaxies form and evolve in different environments across cosmic time. It is well known that strong observational differences exist between the morphology, colour and star formation of galaxies in field-like environments and in rich clusters, particularly at low ($z \lesssim 1$) redshifts (e.g. Dressler 1980; Butcher & Oemler 1984; Poggianti et al. 2001, 2008; Postman et al. 2005; Tran et al. 2005; Cooper et al. 2007, 2008; Lidman et al. 2008; Patel et al. 2009; Bauer et al. 2011). For instance, present-day clusters are dominated by galaxies with elliptical or S0 morphologies, while spirals dominate low-density, field-like environments (e.g. Dressler 1980; Postman & Geller 1984; Norberg et al. 2002; Goto et al. 2003; Blanton et al. 2005; Postman et al. 2005; Desai et al. 2007; Wolf et al. 2007; Ball, Loveday & Brunner 2008).

Most previous studies of galaxy environment are two-dimensional and subject to large uncertainties from projection effects, particularly in clusters where environmental effects are expected to be strongest. Truly understanding the role of galaxy environment on galaxy evolution requires a three-dimensional analysis that considers location in the 'projected' phase space (PPS) of clustercentric radius and line-of-sight velocity.

Recent simulations (e.g. Mahajan, Mamon & Raychaudhury 2011; Oman, Hudson & Behroozi 2013) have demonstrated that a galaxy's orbital history is predictive of the region in phase space that it occupies. In particular, infalling galaxies can be distinguished from galaxies in the virialized cluster core. Thus, it is possible to infer the assembly history of galaxy clusters by correlating phase space to other observable galaxy properties.

In the last few years, galaxy phase space has been exploited by several authors in efforts to understand galaxy properties like star formation and gas stripping (Hernández-Fernández et al. 2014), quenching time-scales (Muzzin et al. 2014; Taranu et al. 2014), H I stripping in galaxies (Jaffé et al. 2015) and galaxy dust temperatures (Noble et al. 2016).

Here, we present our own study of phase space in the A901/2 multicluster system at $z \sim 0.165$. This study jointly exploits two complementary observing campaigns focused on A901/2, the OSIRIS Mapping of Emission-line Galaxies in A901/2 (OMEGA) survey (Chies-Santos et al. 2015; Rodríguez del Pino et al. 2017), which measured redshifts from the Hα and [N II] emission lines of galaxies in A901/2, and the Space Telescope A901/2 Galaxy Evolution Survey (STAGES; Gray et al. 2009). These surveys yield complementary information about galaxy structure and star formation history.

In Section 2, we combine multiple galaxy redshift surveys to assemble a representative sample of 856 galaxies complete in stellar mass down to $10^{8.5}$ M$_\odot$. In Section 3 we outline our phase-space analysis. In Section 4 we investigate how galaxy properties vary across phase space and stellar mass. By comparing galaxy properties in regions of the PPS that statistically separate the infalling population from the population of the virialized region, we can attempt to disentangle which physical processes are influencing galaxies at various points during their accretion history on to the clusters. We discuss the broader implications of our results in Section 5, and in Section 6 we summarize our findings.

We adopt a flat Λ cold dark matter cosmology with $\Omega_\Lambda = 0.7$ and $H_0 = 70$ km s^{-1} Mpc^{-1}. We use Vega magnitudes throughout the paper.

2 DATA AND SAMPLE SELECTION

The multiwavelength STAGES survey covers the A901/2 system of four subclusters at $z \sim 0.165$. The available photometry includes the 17-band Classifying Objects by Medium-Band Observations (COMBO-17) survey (Wolf et al. 2003), covering 31.5×30.0 arcmin^2 ($\sim 5.3 \times 5.1$ Mpc^2). Additionally, *F606W* (*V*-band) *Hubble Space Telescope* (*HST*) Advanced Camera for Surveys imaging was obtained by Gray et al. (2009) covering >90 per cent of the COMBO-17 footprint, with gaps only at the outer edge (see geometric coverage in fig. 2 of Gray et al. 2009). 24 μm photometric coverage from *Spitzer* (Bell et al. 2007), and X-ray data from *XMM–Newton* (Gilmour et al. 2007) are also available. Hubble morphological types were derived by Wolf et al. (2009) from visual classification of the *HST* images.

Photometric redshifts (Wolf et al. 2003) and stellar masses (Borch et al. 2006) have been calculated from the COMBO-17 spectral energy distributions (SEDs). Galaxies have been grouped into one of three SED categories ('Blue Cloud', 'Dusty Red' or 'Old Red') by Wolf, Gray & Meisenheimer (2005) based on application of a red sequence cut suggested by Bell et al. (2004) for COMBO-17. 'Blue Cloud' galaxies are the star-forming galaxies on the blue side of the cut. 'Old Red' galaxies are dust-free red sequence galaxies with $E(B - V) < 0.1$. 'Dusty Red' galaxies are red sequence galaxies with $E(B - V) > 0.1$.

The SED-type naming convention is somewhat misleading as 'Dusty Red' galaxies do not contain more dust than 'Blue Cloud' galaxies, but their ongoing star formation is confined to more dust obscured regions. Wolf et al. (2005, 2009) demonstrated the 'Dusty Red' galaxies are actively forming stars at rates ~ 4 times lower than 'Blue Cloud' galaxies at fixed mass. See Rodríguez del Pino et al. (2017) for additional discussion of these SED types.

Our cluster data set further includes redshifts derived from spectroscopic, prism and narrow-band imaging techniques. These redshifts are discussed below in detail.

2.1 Spectroscopic redshifts

Spectroscopic follow-up of targeted galaxies was carried out with the 2-degree Field (2dF) spectrograph on the Anglo-Australian Telescope and the Very Large Telescope (VLT) Visible Multi-Object Spectrograph (VIMOS) instrument.

The 2dF observations (Gray et al. 2009) prioritized galaxies in the multicluster photometric redshift space having *R*-band magnitude $m_R < 20$ and ultimately yielded redshifts for 356 galaxies. The 2dF redshifts (z_{2dF}) were measured from the Ca H & K absorption features and cross-correlation of the spectra with templates. The VIMOS campaign (Bösch et al. 2013) provides spectra for 200 $M_\star > 10^{8.5}$ M$_\odot$ galaxies having visually confirmed disc components in the *HST* images, a star-forming SED and an inclination angle $i > 30°$. VIMOS redshifts (z_{VIMOS}) were measured from emission lines in 188 cases and absorption lines in the other 12 cases.

Gray et al. (2009) report a redshift accuracy for 2dF of $\Delta_z = 0.00149$. Bösch et al. (2013) find a VIMOS redshift accuracy of $\Delta_z = 0.00019$, based on 16 galaxies included in more than one mask. For the 39 galaxies with redshifts from both surveys, the average of the 2dF and VIMOS redshifts is adopted.

2.2 Prism redshifts

Additional optical spectra were acquired with the Inamori Magellan Areal Camera and Spectrograph (IMACS) on the Baade I 6.5-m
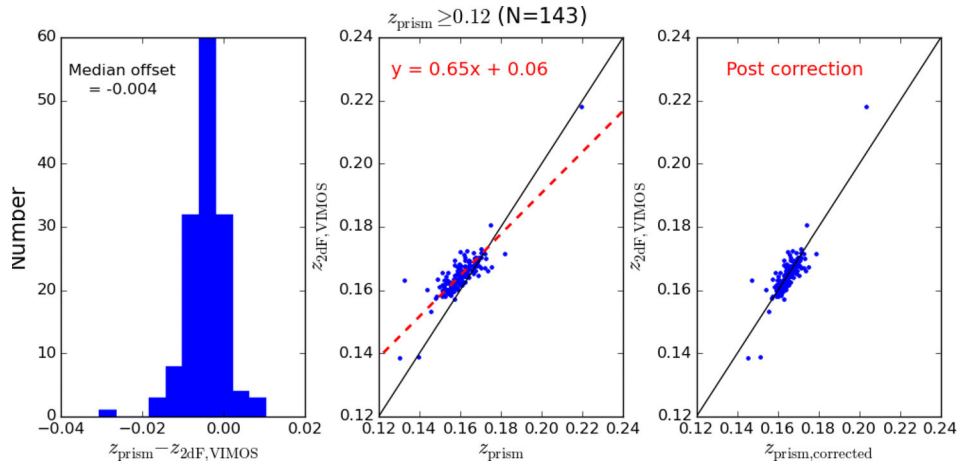
Figure 1. Comparison of the spectroscopic and prism redshifts for a subset of 143 galaxies having both kinds of redshifts. The left-hand panel shows the distribution of offsets between the spectroscopic and prism redshifts. The middle panel shows that the offset is redshift dependent. The solid line is $y = x$. The dashed line is a fit to the data. In the right-hand panel, we have used the fit from the middle panel to recalibrate the prism redshifts to better match the spectroscopic redshifts.

telescope at Las Campanas following the prism spectroscopy method devised by the Prism Multi-object Survey (PRIMUS; Coil et al. 2011) team. IMACS can observe ∼2500 objects simultaneously in a 0.18 deg^2 field of view, yielding more simultaneous spectra than traditional spectroscopic methods but at lower spectral resolving power ($R \approx 40$). The galaxies for which successful redshifts are observed with this approach are disproportionately red, massive and have early Hubble types.

The accuracy of the prism redshifts (z_{prism}) is evaluated with the subset of 143 sources with spectroscopic redshifts and $z_{prism} \geq 0.12$ (note the prism redshifts catastrophically disagree with the spectroscopic redshifts for $z_{prism} < 0.12$). The left-hand panel of Fig. 1 shows the prism redshifts are systematically lower than the spectroscopic redshifts by a median shift of 0.004. The middle panel indicates this offset has a redshift dependence that can be modelled as a straight line. Corrections derived from a linear model are applied to all prism redshifts so they better match the spectroscopic redshifts. The post-correction 1σ redshift scatter is ∼0.0035 for this subset.

2.3 Emission-line redshifts from OMEGA

OMEGA is based on a 90 h ESO Large Programme survey with the Optical System for Imaging and low Resolution Integrated Spectroscopy (OSIRIS) instrument (Cepa 2013) on the 10.4-m Gran Telescopio Canarias (GTC) telescope. The survey was designed to yield deep, spatially resolved emission-line images covering the H α and [N II] lines ($\lambda_{obs} = 7595$–7714 Å) for galaxies in the STAGES multicluster. OMEGA covers $\simeq 658$ arcmin^2, ∼70 per cent of the COMBO-17 footprint. Furthermore, 95 per cent of the OMEGA survey area is also covered by STAGES *HST* imaging (see fig. 1 of Chies-Santos et al. 2015 for a detailed description of the survey geometry).

Low-resolution, 14 Å full width at half-maximum (FWHM) emission-line spectra containing 36–48 data points each were generated from the Fabry–Pérot narrow-band imaging using two different apertures. The radius of the aperture corresponds to 2.5 times the second central moment of the *F606W* light distribution in the STAGES catalogue. The diameter of the second, smaller aperture matches the 1.2 arcsec FWHM point spread function (PSF) of the OSIRIS tunable-filter imaging. The spectra have an absolute

wavelength calibration of ∼1 Å, equal to ∼7 per cent of the instrumental resolution (Weinzirl et al. 2015). From the OMEGA spectra, redshifts, H α fluxes ($f_{H\alpha}$), [N II] fluxes (if detected) and H α equivalent widths ($W_{H\alpha}$) are measured via Bayesian Markov chain Monte Carlo (MCMC) techniques. Chies-Santos et al. (2015) and Rodríguez del Pino et al. (2017) provide details on the survey implementation and spectral fitting.

The OMEGA sample of emission-line galaxies is defined with cuts in H α flux ($f_{H\alpha} \geq 3 \times 10^{-17}$ erg s^{-1} cm^{-2}), H α equivalent width ($W_{H\alpha} \geq 3$ Å) and photometric redshift. All sources in OMEGA that meet the cuts in flux and equivalent width, including contaminants and spurious detections, have emission-line redshifts (z_{OMEGA}) in the narrow range [0.150, 0.176]. A cut in photometric redshift is necessary to isolate the true members of A901/2. We choose to restrict photometric redshift to the range [0.126, 0.200], which was derived by widening the [0.150, 0.176] range by the 3σ uncertainty (0.024) in photometric redshift for a source with *R*-band magnitude 20.5, the median brightness of OMEGA detections (see also Rodríguez del Pino et al. 2017).

Galaxy spectra meeting the cuts in $f_{H\alpha}$, $W_{H\alpha}$ and photometric redshift are visually inspected for quality. Each spectrum is reviewed independently by three classifiers. Spectra flagged two or more times for poor quality are removed from further consideration. After visual classification, there are 439 large-aperture galaxy spectra in which H α is detected (321 of these also show [N II]) and 360 PSF-aperture spectra containing both H α and [N II].

Among galaxies with existing redshifts from 2dF/VIMOS, OMEGA detects all galaxies having rest frame $B - V < 0.7$. More importantly, the majority (270) of the OMEGA detections did not previously have spectroscopic or prism redshifts. The new redshifts are an important addition because OMEGA preferentially selects a population of blue star-forming galaxies that is under-represented in the 2dF and prism redshifts (note the VIMOS redshift sample was selected based on a star-forming SED type).

The top panel of Fig. 2 compares the OMEGA redshifts to the spectroscopic redshifts for the 136 galaxies in OMEGA meeting the cuts in $f_{H\alpha}$, $W_{H\alpha}$ and photometric redshift. The agreement is almost perfect for sources with $W_{H\alpha} \geq 10$ Å and some additional sources with lower equivalent width. There are 44 sources of low equivalent width ($3 \leq W_{H\alpha} < 10$ Å) having OMEGA redshifts offset

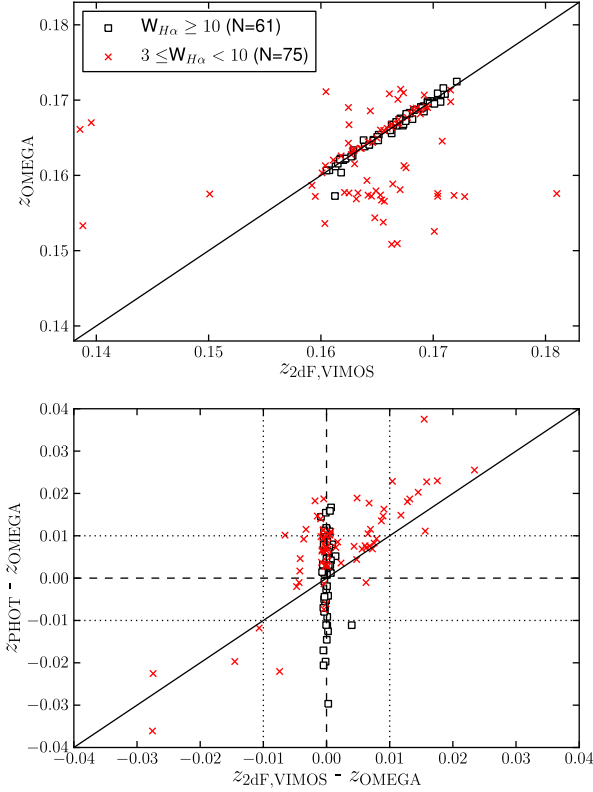Comparison of 2dF, VIMOS redshifts versus OMEGA redshifts

Figure 2. Comparison of the OMEGA, spectroscopic and photometric redshifts for the 136 sources in OMEGA that also have spectroscopic redshifts from 2dF and/or VIMOS. Top panel: redshifts in OMEGA versus those from 2dF/VIMOS. Bottom panel: the difference of the OMEGA redshifts from the spectroscopic redshifts (*x*-axis) and the COMBO-17 photometric redshifts (*y*-axis). Data points are coded by Hα equivalent width ($W_{H\alpha}$). The dashed and dotted lines show redshift offsets of 0 and ± 0.01, respectively. In both panels, the solid lines indicate equality. The 1σ standard deviation of the redshift bias between 2dF/VIMOS and OMEGA is ~ 0.0082 for $3 \leq W_{H\alpha} < 10$ and ~ 0.00066 for $W_{H\alpha} \geq 10$.

by >0.001 from the spectroscopic measurement, compared to just two at $W_{H\alpha} \geq 10$ Å.

The bottom panel of Fig. 2 compares the offsets of the OMEGA redshifts from the photometric and spectroscopic redshifts ($z_{phot} - z_{OMEGA}$ versus $z_{2dF, VIMOS} - z_{OMEGA}$). Data points on the line of equality in the top panel are now on the dashed $x = 0$ line. The problematic OMEGA redshifts are generally offset from the spectroscopic and photometric redshifts in the same diagonal direction (i.e. they are smaller), suggesting the OMEGA redshifts are inaccurate because of spurious detections or inaccurate emission-line identification.

The 1σ standard deviation of the residuals between the spectroscopic and OMEGA redshifts is ~ 0.00820 for $3 \leq W_{H\alpha} < 10$ and ~ 0.00066 for $W_{H\alpha} \geq 10$. Among the 439 galaxy spectra passing visual inspection, there are 120 with $3 \leq W_{H\alpha} < 10$ and 319 with $W_{H\alpha} \geq 10$, so the average weighted error in the OMEGA redshifts is ~ 0.0027.

2.4 Definition of parent and redshift samples

The sample of galaxies used for the PPS analysis is presented here. We first define a parent sample S1 of 1438 STAGES galaxies from

cuts in stellar mass ($M_{\star} \geq 10^{8.5}$ M$_{\odot}$) and photometric redshift [0.126, 0.200] to match the OMEGA sample (Section 2.3). We further define selection criteria using STAGES catalogue flags from Gray et al. (2009) to require galaxies be in the COMBO-17 footprint (COMBO_FLAG ≥ 3) and to have been detected in the *HST* imaging (STAGES_FLAG ≥ 2). Most (~ 87 per cent) of S1 galaxies are 'cluster member' galaxies having STAGES catalogue flag COMBO_FLAG ≥ 4. This selects all galaxies according to the definition of 'cluster' in fig. 13 of Gray et al. (2009). Fig. 3 shows histogram distributions for stellar mass, colour, SED type and morphology of S1. The mass function of S1 does not turn over above $M_{\star} \geq 10^{8.5}$ M$_{\odot}$. Gray et al. (2009) show STAGES is >90 per cent complete for $R < 23.5$, which corresponds to $M_{\star} \geq 10^{9}$ M$_{\odot}$ (Maltby et al. 2010). The completeness of our sample should be somewhat less than 90 per cent given our choice of mass cut.

Some of the OMEGA detections (Section 2.3) are excluded from S1 because they either fall below the stellar mass limit or they have COMBO_FLAG $=2$. S1 contains 397/439 OMEGA galaxies with large-aperture spectra and 329/360 galaxies with PSF-aperture spectra.

Fig. 4 shows the redshift completeness fractions for sample S1 in terms of stellar mass, colour, SED type and morphology for the different redshift measures. The inherent selection bias of each redshift technique is apparent in columns 1–3. The spectroscopic and prism redshift samples have relatively few blue, star-forming galaxies, which is the dominant population detected by OMEGA.

Sample S2 is constructed from the 856 galaxies with redshift measurements. The best available redshift, in descending order of spectral resolution (2dF/VIMOS, OMEGA and prism spectroscopy), is chosen for each galaxy. Column 4 of Fig. 4 represents sample S2. The redshift completeness in stellar mass is >50 per cent for $M_{\star} > 10^{9.5}$ M$_{\odot}$, is >40 per cent across colour and is >50 per cent for Hubble types E to Sc. Including galaxies uniquely detected by OMEGA in this analysis increases the number of redshifts by ~ 47 per cent over what just VIMOS/2dF and prism spectroscopy provide alone.

Sample S2, while limited in completeness, benefits from combining the sensitivities of each of the three redshift surveys it was built from. The result is a sample covering a much better range of galaxy properties (colour, SED type and morphology). We will use this sample throughout the rest of the paper. Sample S2 contains 856 galaxies, of which 359 have redshifts based on 2dF/VIMOS spectroscopy, 273 based on OMEGA data and 224 based on prism observations.

3 PHASE SPACE

For the purposes of the dynamical analysis in this paper we subdivide the field into regions surrounding four main subclusters. Here we are guided by the luminosity-weighted maps of photometrically selected cluster members and peaks in the gravitational lensing mass maps (Gray et al. 2002; Heymans et al. 2008).

For sample S2, the positions of galaxies in PPS are calculated relative to the nearest subcluster in A901/2. Specifically, we use the subclustercentric radius normalized by the subcluster virial radius (R_p/R_{200}) and the peculiar line-of-sight rest-frame velocity normalized by the subcluster galaxy velocity dispersion ($\Delta V_{los}/\sigma_{scl}$). We adopt the subcluster centres and R_{200} from the 'one-halo' models fitted by Heymans et al. (2008). We use the definition

$$\Delta V_{los} = \frac{c(z - z_{scl})}{(1 + z_{scl})}, \qquad (1)$$

where c is the speed of light and z_{scl} is the subcluster redshift.
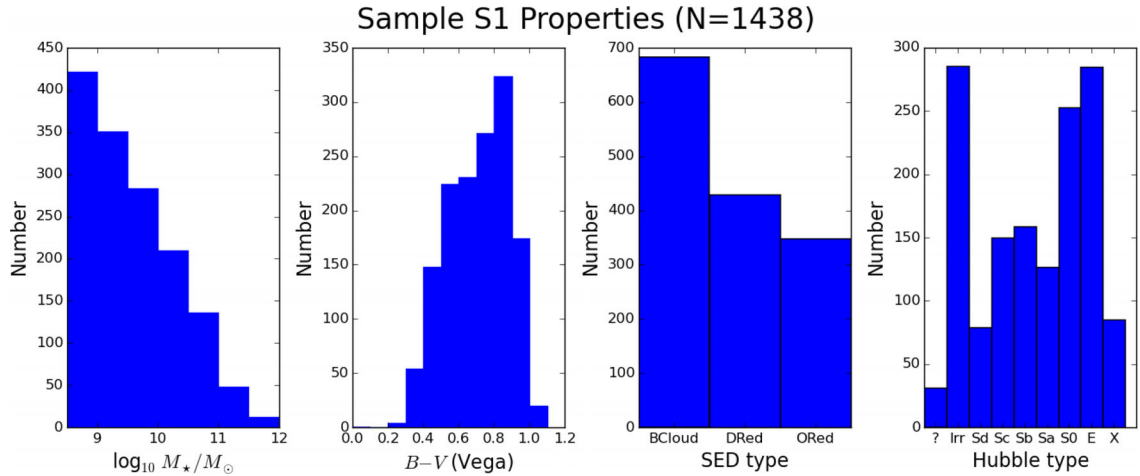
Sample S1 Properties (N=1438)

Figure 3. Distributions of stellar mass, colour and Hubble type for sample S1 with $M_\star \geq 10^{8.5}$ M$_\odot$ and photometric redshift in the range [0.126, 0.200]. In the third panel from the left, the SED types are abbreviated as BCloud ('Blue Cloud'), DRed ('Dusty Red') and ORed ('Old Red'). The fourth panel shows the Hubble types derived from the classifications of Wolf et al. (2009), where '?' means unclassifiable and 'X' means resolved but compact.

Mean subcluster redshifts $z_{\rm scl}$ and velocity dispersions $\sigma_{\rm scl}$ are calculated with the biweight estimators of location and scale (Beers, Flynn & Gebhardt 1990) following the procedure employed by Bösch et al. (2013) in their previous calculations for A901/2. These calculations warrant repeating because there are now significantly more galaxy redshifts (856) than the 200 VIMOS redshifts used in Bösch et al. (2013). Galaxies are initially assumed to be members of the nearest subcluster in terms of projected distance. Subsequent iterations use 3σ clipping to filter outliers until convergence where all remaining galaxies fall into the 3σ velocity-dispersion interval of their subcluster.

At this point it is important to consider how the relatively large uncertainties of the OMEGA and prism redshifts ($\delta z \sim 0.003$ or $\delta v \sim 900$ km s^{-1}) may affect the velocity dispersion determination and our subsequent analysis. Reassuringly, the values we obtain agree very well with the ones published by Bösch et al. (2013): three out of the four $\sigma_{\rm scl}$ values agree within 1σ error, and the fourth is $\sim 1.8\sigma$ away. Moreover, we detect no bias between our measurements and theirs. For additional peace of mind, we have also calculated $\sigma_{\rm scl}$ using the more accurate 2dF and VIMOS redshifts only. We find that the subcluster redshifts $z_{\rm scl}$ change by less than 0.001 in all cases, and $\sigma_{\rm scl}$ changes by less than 10 per cent in three out of four cases (the exception is the SW Group, where the uncertainty in the 2dF/VIMOS value is very large due to small number statistics, and the different values agree well within the errors). We are therefore satisfied that using the complete set of redshifts does not bias the measured redshifts or velocity dispersions. Because the formal errors are smaller when using the larger galaxy sample, we have carried our analysis using the $z_{\rm scl}$ and $\sigma_{\rm scl}$ values we calculated. However, our conclusions would not change had we used the compatible values estimated by Bösch et al. (2013).

Table 1 lists the resulting subcluster redshifts and velocity dispersions along with the adopted centres and dark halo parameters (R_{200}, M_{200}) from Heymans et al. (2008). Note that the derived physical parameters of the clusters (cluster centres, R_{200} and M_{200}) were not determined from the velocity dispersion measurements but from the lensing work of Heymans et al. (2008). Velocity dispersions are affected by the dynamical state of the structures, and determining subcluster masses and radii from $\sigma_{\rm scl}$ is very uncertain and potentially biased for non-virialized clusters and/or in the presence of substructure.

Fig. 5 shows the spatial distribution of sample S2 in relation to the subcluster centres. In the top panel, galaxies are coded by the adopted redshift source. In the bottom panel, galaxies are coded by the nearest cluster centre. Phase-space parameters ($R_{\rm p}/R_{200}$ and $\Delta V_{\rm los}/\sigma_{\rm scl}$) are calculated relative to the halo parameters of the nearest cluster, a strategy that maximizes the number of galaxies in the central virialized region. Potential concerns with this strategy are the effects of overlapping R_{200}, cluster centring errors and contamination between clusters. The R_{200} overlap for A901a and A901b causing 20 galaxies to fall inside both R_{200} radii. Our cluster membership scheme equally divides the overlapping galaxies between A901a and A901b. The close proximity of A901a and A901b should not seriously bias the phase-space analysis because their halo parameters are similar, their R_{200} agree to within 0.01 Mpc and their $\sigma_{\rm scl}$ differ only by 10 per cent (Table 1).

We use the PPS to distinguish cluster galaxies in the virialized region from infalling galaxies with the aim of constraining which environmental processes are relevant in A901/2. Following Mahajan et al. (2011) and Jaffé et al. (2015), we use triangular regions to represent the inner virialized region. Our fiducial boundary (B1), $R_{\rm p}/R_{200} \leq 1.2$ and $|\Delta V_{\rm los}/\sigma_{\rm scl}| \leq 1.5 - 1.5/1.2 \times R_{\rm p}/R_{200}$, is used by Jaffé et al. (2015) in the study of a cluster that is comparable in mass (7.7×10^{14} M$_\odot$) to A901a and at a comparable redshift ($z = 0.2$). The second boundary (B2), $R_{\rm p}/R_{200} \leq 0.5$ and $|\Delta V_{\rm los}/\sigma_{\rm scl}| \leq 2.0 - 2.0/0.5 \times R_{\rm p}/R_{200}$, extends to higher $\Delta V_{\rm los}/\sigma_{\rm scl}$. While B2 is set somewhat arbitrarily, it defines a virialized region 45 per cent smaller in area than B1; its purpose is to provide an estimate of how sensitive the phase-space analysis is on the definition of the virialized region.

Fig. 6 is a PPS diagram with these boundaries overlaid, stacking together the four subclusters in A901/2. B1 and B2 are represented with dashed and dotted lines, respectively. Galaxies are again coded by adopted redshift source. B1 encloses 210 galaxies while B2 encloses 70 galaxies.

An important caveat to keep in mind is the potential effect of spatial incompleteness on the stacked PPS diagram. Sources of spatial incompleteness include, for example, the finite OMEGA footprint and 2dF fibre collisions in crowded virialized regions. While Fig. 5 shows all clusters are well populated within R_{200}, spatial incompleteness is evident beyond R_{200}, particularly for A902 and the SW Group. Given the narrow redshift range covered by the

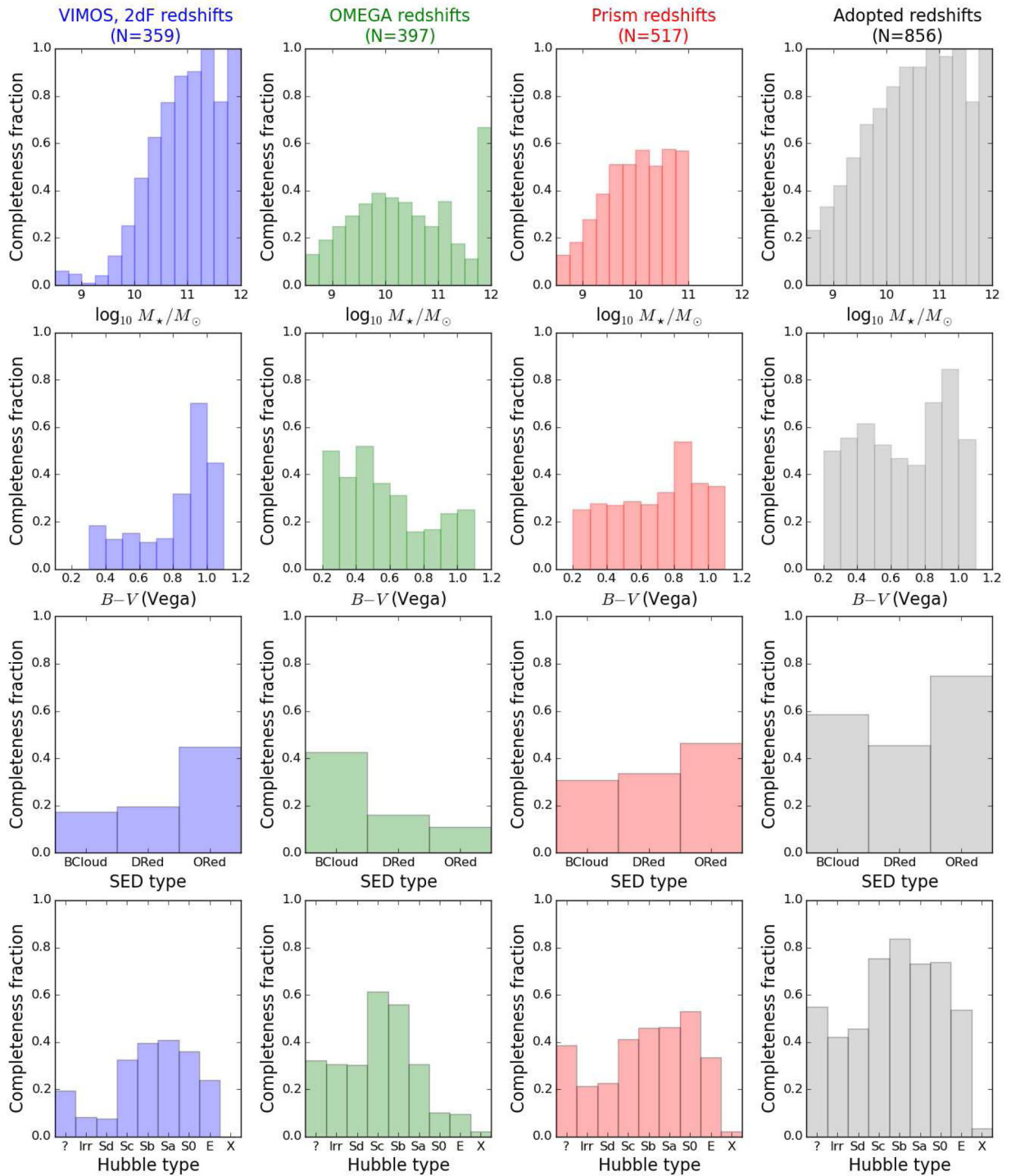## Redshift Completeness of Sample S1 (N=1438)

Figure 4. The redshift completeness fraction of the mass and photometric redshift selected sample, S1, for stellar mass, colour, SED type and morphology. The SED types and morphologies were classified by Wolf et al. (2009). Columns 1–3 represent the 2dF/VIMOS redshifts, OMEGA redshifts and prism redshifts, respectively. Column 4 represents the best available redshifts adopted in descending order (column 1, column 2 and column 3) of spectral resolution. The SED and Hubble type labels are as in Fig. 3.

system, possible incompleteness in the redshift sampling is not expected to be a significant concern.

Visual inspection of Fig. 6 reveals that the PPS diagram of the A901/902 system does not show the clear 'trumpet shape'

expected for spherically collapsing systems (e.g. Regos & Geller 1989; Diaferio & Geller 1997). This could be due (at least in part) to the relatively large redshift uncertainties affecting a significant fraction of the galaxy sample, but it could also be the consequence

Table 1. Subcluster redshifts, velocity dispersions and dark halo parameters in A901/2.

Subcluster	RA (°)	Dec. (°)	z_{scl}	σ_{scl} (km s^{-1})	R_{200} (Mpc)	M_{200} (10^{14} M$_\odot$)
A901a	149.1099	−9.9561	0.1631	878^{+17}_{-27}	$0.84^{+0.06}_{-0.07}$	$1.3^{+0.3}_{-0.3}$
A901b	148.9889	−9.9841	0.1641	937^{+15}_{-22}	$0.83^{+0.06}_{-0.07}$	$1.3^{+0.3}_{-0.3}$
A902	149.1424	−10.1666	0.1656	808^{+13}_{-20}	$0.56^{+0.08}_{-0.09}$	$0.4^{+0.2}_{-0.2}$
SW Group	148.9101	−10.1719	0.1693	585^{+25}_{-37}	$0.63^{+0.07}_{-0.08}$	$0.6^{+0.2}_{-0.2}$

Note. The cluster redshifts and velocity dispersions (z_{scl}, σ_{scl}) are determined in Section 3. The cluster centres and dark halo parameters (R_{200} and M_{200}) come from Heymans et al. (2008), and are not based on the values of the subcluster velocity dispersions (see text for details).

of the complex nature and dynamical state of the whole system and each individual subsystem. If each individual subcluster could be considered as not disturbed, we should be able to see a 'trumpet shape' when stacking the four distributions, provided we are able to cleanly separate members of each structure (which is clearly not the case due to complex spatial and redshift projection effects). Because it is highly likely that the four subclusters are interacting and possibly merging with each other, it is hard to believe that they are individually unperturbed. Redshift uncertainties would, no doubt, contribute to blurring any putative underlying 'trumpet shape', but we think the complexity of the system, which compounds dynamical and projection effects, is the dominant reason why we do not see such a shape. The distribution on this diagram of the galaxies with 2dF/VIMOS spectroscopy (for which the redshift uncertainties are much smaller) is not significantly different from that of the galaxies with prism or OMEGA redshifts. This suggests that even if we had *perfect* redshifts for the whole sample, a clear 'trumpet shape' would not arise.

4 ENVIRONMENTAL EFFECTS ACROSS PROJECTED PHASE SPACE

4.1 Imaging properties

For sample S2, we look for differences in imaging-derived galaxy properties (stellar mass, rest-frame colour, structure, Hubble type and SED type) between the virialized and non-virialized regions of the PPS. The stellar masses, colours and SED types were derived from the COMBO-17 photometry, and Hubble types were derived from the *HST* images (Section 2). The structural parameters include galaxy-wide Sérsic (1963) indices and half-light radii measured from the *HST* images by Gray et al. (2009). Sérsic index is interesting because it broadly distinguishes dynamically cold, discy stellar structures from dynamically hot ones (Andredakis, Peletier & Balcells 1995; de Jong 1996; Khosroshahi, Wadadekar & Kembhavi 2000, and more recently e.g. Weinzirl et al. 2011, 2014).

The top row of Fig. 7 shows the cumulative distributions of stellar mass, rest-frame $B - V$ colour, Sérsic index and half-light radius inside and outside the virialized regions, as defined by our fiducial boundary B1 (Section 3, Fig. 6). Kolmogorov–Smirnov (KS) tests are used to compare the statistical significance of apparent disparities across phase space. For stellar mass, there is a 3.3σ difference ($p = 0.0011$) such that the galaxies in the virialized region are more massive. There is a significantly stronger (4.4σ, $p = 1.0 \times 10^{-5}$) disparity in colour implying these central galaxies are redder overall. Sérsic index and half-light radius show less significant differences. At the 2.6σ level, virialized-region galaxies tend to have higher Sérsic indices (i.e. they are less discy) than galaxies outside the virialized region. Virialized-region galaxies may also be slightly larger in half-light radius (1.7σ).

Galaxy colour (e.g. Bell et al. 2004), galaxy size (e.g. Lange et al. 2015) and Sérsic index (e.g. Graham & Guzmán 2003; Kormendy et al. 2009) all scale with galaxy luminosity (i.e. stellar mass). Since galaxies in the virialized region are more massive (the median stellar mass is $10^{10.03}$ M$_\odot$ in the virialized region versus $10^{9.76}$ M$_\odot$ in the non-virialized region), it is important to consider if it is mass, rather than environmental effects, driving the differences in the other three properties.

The middle and bottom rows of Fig. 7 repeat the KS tests of the virialized and non-virialized regions for the sample after subdivision into bins above and below the 50th percentile in stellar mass ($M_{50} = 10^{9.85}$ M$_\odot$) within sample S2. For the lower mass bin ($M_\star \leq M_{50}$), $B - V$ and Sérsic index show differences across the PPS at marginal significance that can probably be accounted for by stellar mass. For the higher mass bin ($M_\star > M_{50}$), there is no evidence for changes in stellar mass, Sérsic index or half-light radius. This distributions of $B - V$, however, differ very significantly ($>3\sigma$).

The change in $B - V$ but not stellar mass in the $M_\star > M_{50}$ row of Fig. 7 suggests the 4.4σ result in the top row for $B - V$ is not driven entirely by mass. Fig. 8 shows the colour–magnitude diagrams and distributions of $B - V$ colour in the two phase-space bins. The colour–magnitude diagrams (left-hand and middle panels) show proportionately fewer galaxies with $B - V < 0.7$ at fixed M_V in the virialized region (left) compared to the non-virialized region (middle). Across all luminosities, the non-virialized region contains a factor of 1.6 more galaxies with $B - V < 0.7$ than the virialized region. Noteworthy in the non-virialized region is a population of spirals with $M_V \leq -21$ (i.e. $M_\star \geq 10^{10}$ M$_\odot$) that is absent in the virialized region. Thus, the strong colour difference in Fig. 7 arises from a deficit of blue ($B - V < 0.7$), high-mass ($M_\star > 10^{9.85}$ M$_\odot$) galaxies (mostly spirals) in the virialized region.

A similar analysis is conducted to assess the influence of stellar mass on morphology and the SED type. The left column of Fig. 9 shows the histograms of Hubble type in three different stellar mass bins (all masses, $M_\star \leq M_{50}$ and $M_\star > M_{50}$). Visual inspection of the histogram for all masses shows irregular galaxies are ~30 per cent less common in the virialized region and that S0s are ~25 per cent more common. A χ^2 test (rather than KS, since these are discrete quantities) for Hubble types E to Irr, however, gives a p-value of 0.216 (1.2σ), indicating these differences are not statistically meaningful. The middle and bottom panels show Hubble type has even less variation across the PPS once isolated into low- and high-mass bins.

The right-hand column of Fig. 9 addresses the SED type. Across all stellar masses, there is a 4.3σ difference between 'Blue Cloud' and 'Old Red' SED types, such that there are ~50 per cent (~62 per cent) more (fewer) 'Blue Cloud' ('Old Red') galaxies in the non-virialized region. This result is stronger than the result for stellar mass (3.3σ) and comparable to the one for rest-frame
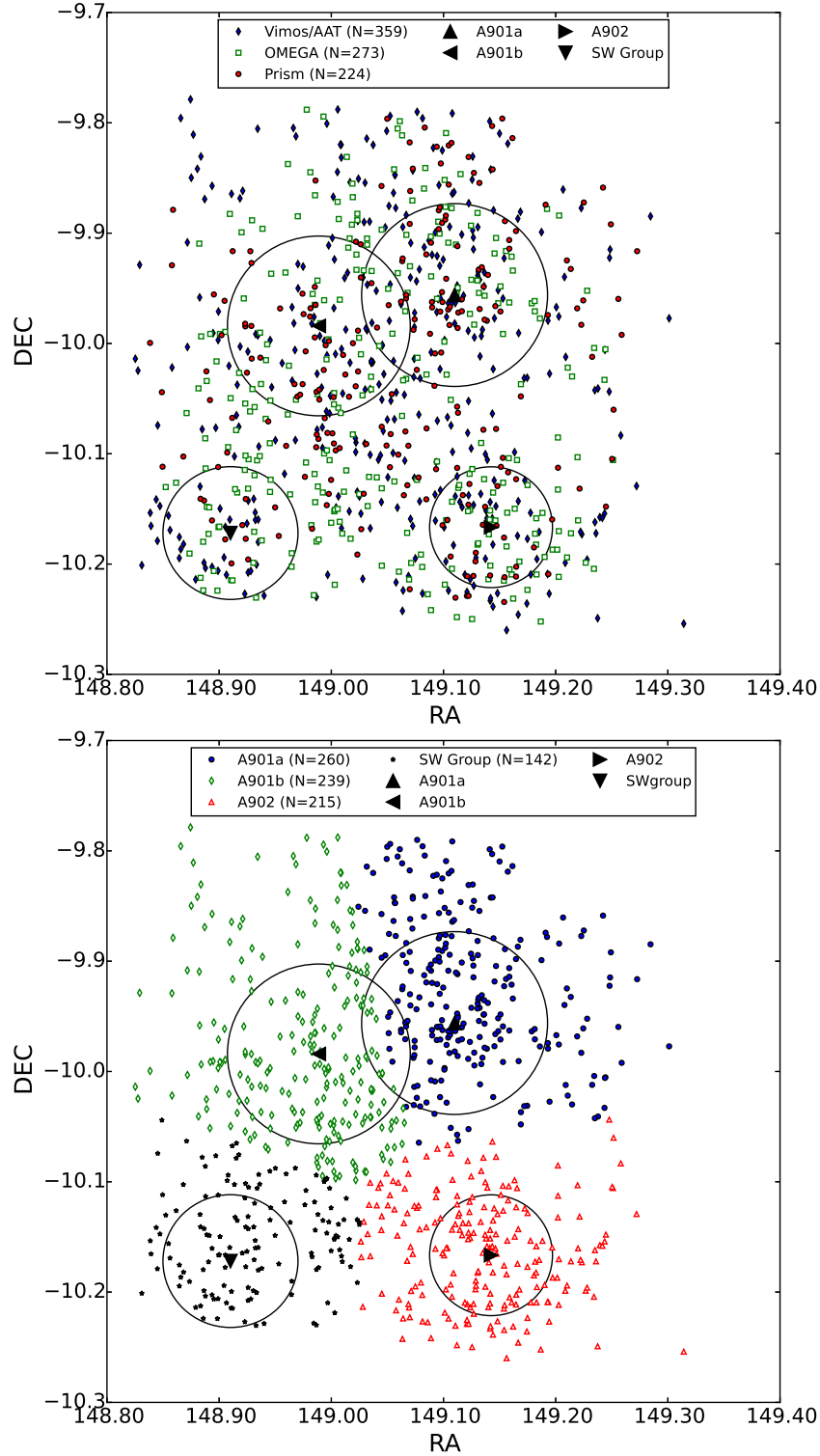
Figure 5. The top panel shows the spatial distribution of the 856 galaxies in sample S2 coded by the source of the adopted redshifts. The four subclusters are separately labelled, and their spheres of influence (R_{200}) are shown as circles. In the bottom panel, galaxies are colour coded by the nearest cluster centre.

$B - V$ (4.4σ) in Fig. 7. In the $M_\star \leq M_{50}$ mass bin, this difference drops to 2.6σ but is still more significant than the change in stellar mass across the PPS in the low-mass bin (2.1σ). In the $M_\star > M_{50}$ mass bin, the difference for SED type is 2.3σ, much higher than the 0.90σ found for stellar mass. Thus, SED type evolves across the PPS similar to rest-frame $B - V$.

The KS and χ^2 tests presented in this section have focused on the fiducial boundary B1. The test statistics are summarized in columns 3–5 of Table 2. Similar and qualitatively consistent results are found for alternate boundary B2, which defines a more conservative virialized region (Section 3). Column 6 lists the test statistics when applying instead boundary B2 without binning by stellar mass.
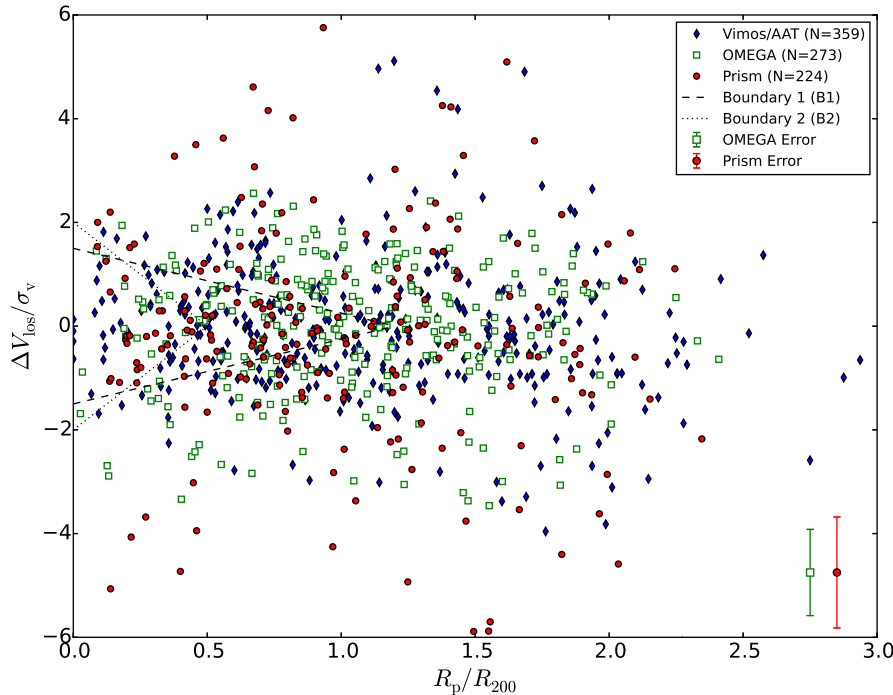
Figure 6. The projected phase space of the 856 galaxies in sample S2 are shown, coded by the source of the adopted redshifts. The four subclusters are stacked together. The dashed and dotted lines denote the two different boundaries used for the virialized region of phase space. The dashed line (boundary 1) is defined by $R_{\rm p}/R_{200} \leq 1.2$ and $|\Delta V_{\rm los}/\sigma_{\rm scl}| \leq 1.5 - 1.5/1.2 \times R_{\rm p}/R_{200}$. The dotted line (boundary 2) is defined by $R_{\rm p}/R_{200} \leq 0.5$ and $|\Delta V_{\rm los}/\sigma_{\rm scl}| \leq 2.0 - 2.0/0.5 \times R_{\rm p}/R_{200}$. There are 210 galaxies inside boundary 1 and 70 galaxies inside boundary 2. The average errors for the OMEGA and prism $|\Delta V_{\rm los}/\sigma_{\rm scl}|$ appear in the lower right, and they reflect the redshift biases relative to the spectroscopic redshifts.

4.2 Emission-line derived properties

In this section, we explore how emission-line properties derived from the OMEGA spectra [gas-phase metallicity, star formation and active galactic nucleus (AGN) emission] vary across the PPS.

4.2.1 Star formation and AGN activity

Cid Fernandes et al. (2010, 2011) demonstrate the utility of using the WHAN diagram ([N II]/Hα versus $W_{\rm H\alpha}$) to discriminate star formation and black hole activity as sources of gas ionization. Fig. 10 shows the WHAN diagram, assuming the standard boundaries from Cid Fernandes et al. (2010), for the subset of 329 OMEGA galaxies in sample S2 whose PSF-aperture spectra have both the Hα and [N II] within the wavelengths probed. There are 198/329 ($\sim$60.2 per cent) galaxies on the 'star forming' side of the diagram, 93/329 ($\sim$28.3 per cent) in the 'Seyfert' area and 38/329 ($\sim$11.6 per cent) in the 'LINER' area.

The significance of the 'star forming' versus 'AGN' classifications in the WHAN diagram can be quantified using the probability distributions for [N II]/Hα and $W_{\rm H\alpha}$ arising from our Bayesian spectral fitting (Section 2.3). The probability that a galaxy is dominated by star formation or AGN emission is calculated based on its position relative to the boundaries in Fig. 10. Galaxies with $\geq$99.7 per cent ($\geq 3\sigma$) probability of being in the star-forming or AGN categories are distinguished in Fig. 10. There are 132 such bona fide star-forming galaxies and 46 such AGN-dominated galaxies.

Table 3 lists the number counts of $\geq 3\sigma$ star-forming and AGN galaxies in different regions of the PPS, as well as in the two stellar mass bins $M_\star \leq M_{50}$ and $M_\star > M_{50}$. The majority of star-forming

(105/132 for B1 and 125/132 for B2) and AGN galaxies (29/46 for B1 and 39/46 for B2) are outside the virialized region. Most star-forming galaxies (108/132) are in the low-mass bin, while the majority (31/46) of AGNs are in the high-mass bin.

A χ^2 test for the numbers of star-forming and AGN galaxies across the PPS using the B1 boundary gives a *p*-value of 0.025 (2.2σ). The same test for B2 gives a similar *p*-value, 0.031 (2.2σ). The χ^2 test across mass bins gives a highly significant *p*-value of 5.0×10^{-10} (6.2σ). Change in the numbers of star-forming and AGN galaxies across phase space is quite weak compared to the change in number counts due to stellar mass.

4.2.2 Metallicity in star-forming galaxies

The [N II]/Hα ratio has been shown (e.g. Denicoló, Terlevich & Terlevich 2002; Pettini & Pagel 2004) to be a robust calibrator of gas-phase metallicity [O/H] for star-forming galaxies. The relation of [N II]/Hα to metallicity is monotonic, and the [N II] and Hα lines can be measured in our moderate-resolution OMEGA spectra. The downside of [N II]/Hα is that its sensitivity to ionization variations (e.g. Nagao, Maiolino & Marconi 2006) means it is only suitable for measuring integrated galaxy abundances. Here, we consider the galaxy-wide [N II]/Hα metallicities of the $\geq 3\sigma$ star-forming galaxies *identified from* PSF-aperture OMEGA spectra in Section 4.2.1 and in Fig. 10 (details of the photometry are in Rodríguez del Pino et al. 2017).

The top left-hand panel of Fig. 11 shows the [N II]/Hα ratio versus stellar mass, colour coded by position in the PPS, with respect to boundary B1. There is a weak trend in [N II]/Hα across stellar mass present for both PPS bins. Moreover, the full range of line ratio is present in the virialized and non-virialized regions. The top
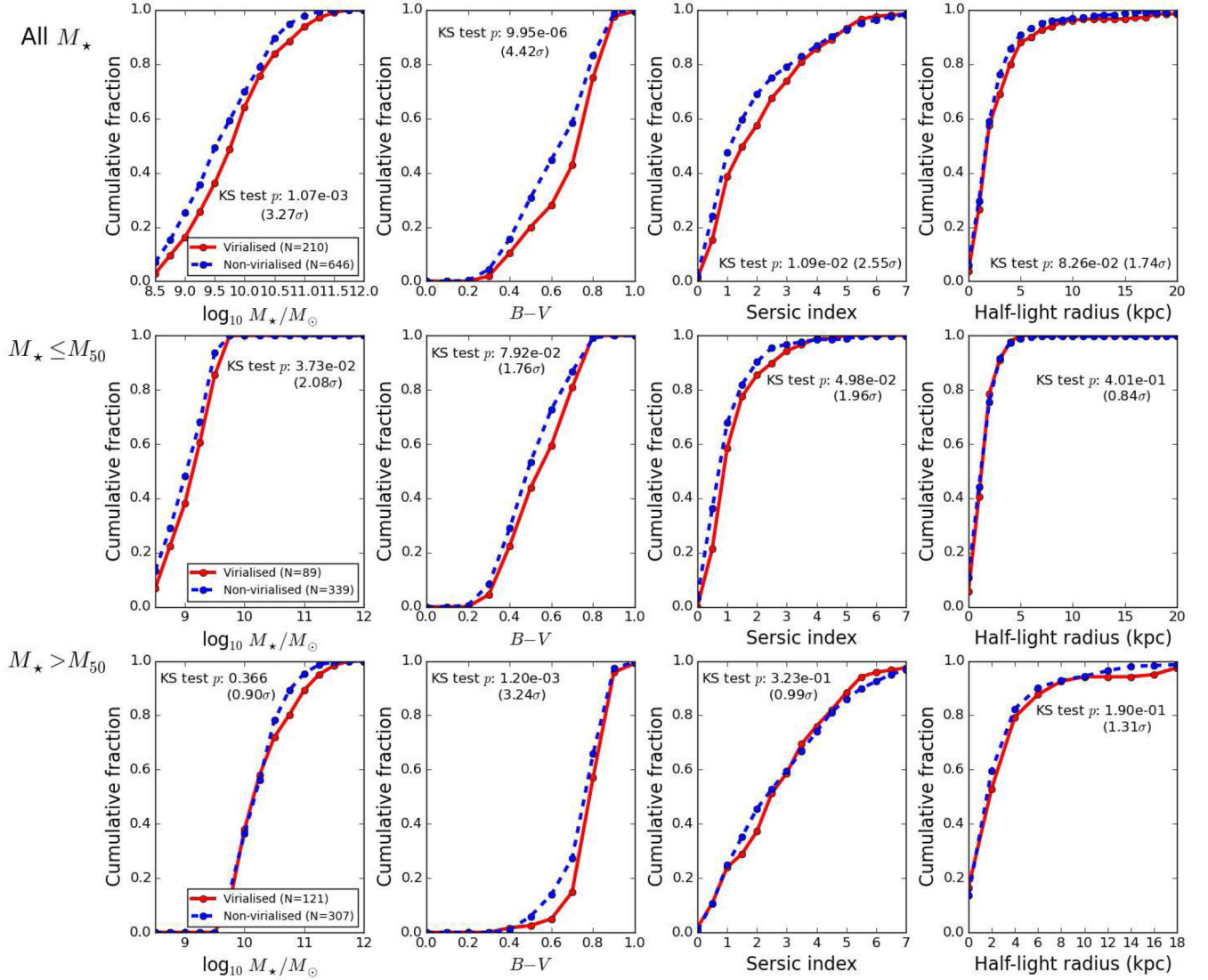
Figure 7. Stellar mass, colour, Sérsic index and half-radius are compared in the virialized and non-virialized regions of the A901/2 system. The virialized region is defined using fiducial boundary B1 (Section 3, Fig. 6). Panel annotations convey the *p*-value significances of Kolmogorov–Smirnov (KS) tests on the distributions in each panel. The top row includes galaxies of all stellar masses. The middle and bottom rows represent subsamples partitioned around the 50th percentile in stellar mass ($M_{50} = 10^{9.85}$ M$_\odot$). Similar results are found when substituting boundary B1 for B2.

right-hand panel of Fig. 11 compares the cumulative distributions for the two PPS bins. A KS test gives a *p*-value 0.81 (0.23σ). There is no evidence that the distribution of [N II]/Hα differs between the two regions.

The bottom row of Fig. 11 repeats the same analysis for the more central PPS boundary B2. The results appear to be more significant for B2 ($p = 0.049$, 2.0σ), and the cumulative line ratio distributions suggest there are more galaxies with low metallicities ([N II]/H$\alpha <$ -1) in the virialized region. However, the significance of the KS test is still only marginal with just 32 bona fide star-forming galaxies in the more conservative virialized region. We conclude that in our data set we do not detect any significant difference in metallicity as traced by [N II]/Hα across the PPS.

4.2.3 Hα specific star formation rate deficit

Using Hα star formation rates (SFR$_{\text{H}\alpha}$) derived from the large-aperture OMEGA spectra of galaxies in sample S2 (Section 2.4),

we look for a change in the way specific SFR$_{\text{H}\alpha}$ (or SSFR$_{\text{H}\alpha}$) scales with stellar mass in the *intracluster* environment. As in Rodríguez del Pino et al. (2017), we convert Hα luminosity to star formation rate using the Kennicutt (1998) relation with an additional mass-dependent dust attenuation correction estimated from fig. 6 of Brinchmann et al. (2004). The conversion is

$$\frac{\text{SFR}_{\text{H}\alpha}}{(\text{M}_\odot \, \text{yr}^{-1})} = 7.9 \times 10^{[-42 + 0.4 \times A_{\text{H}\alpha}(M_\star)]} \frac{L_{\text{H}\alpha}}{(\text{erg s}^{-1})}, \qquad (2)$$

where $A_{\text{H}\alpha}(M_\star)$ is the dust attenuation term.

We define SSFR$_{\text{H}\alpha}$ deficit as the offset relative to the SSFR$_{\text{H}\alpha}$–$M_\star$ relation for field galaxies in Sloan Digital Sky Survey (SDSS; Abazajian et al. 2009); at a given mass, a galaxy with a lower SSFR$_{\text{H}\alpha}$ than the SDSS relation has a positive SSFR$_{\text{H}\alpha}$ deficit. Fig. 12 shows the SSFR$_{\text{H}\alpha}$–$M_\star$ relation for the field (black line) and for our sample (points) of 397 galaxies from S2 with large-aperture OMEGA spectra.
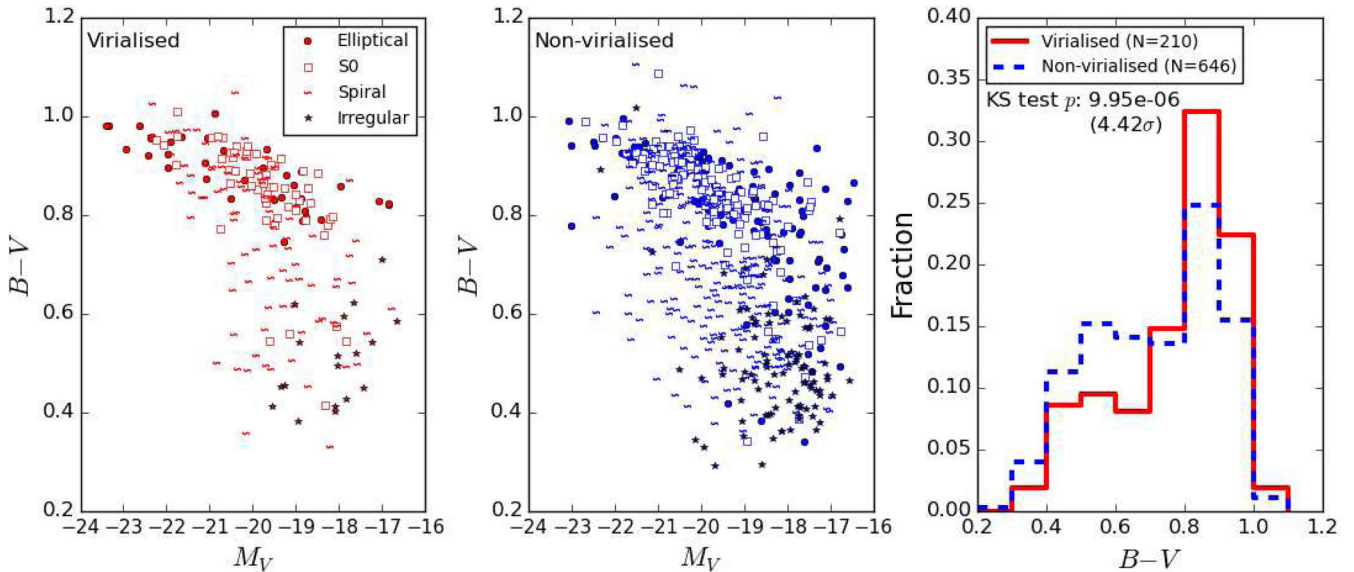
Figure 8. The left-hand and middle panels show the rest-frame $B - V$ colour versus absolute V magnitude diagram for the virialized and non-virialized regions. The right-hand panel shows histograms of colour in the two phase-space bins. Like Fig. 7, the virialized region is defined using fiducial boundary B1.

To compare the star formation deficit of the galaxies in different PPS regions we require an unbiased sample that is not affected by H α flux and equivalent with selection effects. Following the detailed analysis of Rodríguez del Pino et al. (2017), for this comparison we use sample S3, which comprises the 351 OMEGA galaxies lying above the dashed line shown in Fig. 12. This line is parallel to the $SSFR_{H\alpha}$–$M_\star$ relation in the field and defines a region where the H α-detected galaxies are above the flux and equivalent width detection limits of the survey (see Fig. 12 and its caption for more details). While we are only concerned here with the relative offset from the field line shown in Fig. 12 for galaxies in different regions of the PPS, it is clear that there is an overall reduction in SSFR for the complete OMEGA sample relative to the field. This is a result discussed in detail by Rodríguez del Pino et al. (2017) for a similar sample drawn from the OMEGA survey.

The top panel of Fig. 13 shows histograms of the $SSFR_{H\alpha}$ deficit in the virialized and non-virialized regions as defined by boundary B1. A KS test shows no probable difference ($p = 0.98$, 0.03σ) between these distributions. In order to estimate the upper limit on the difference in average $SSFR_{H\alpha}$ between the two regions that our data are able to rule out, we repeat the KS test for a range of relative offsets. The bottom panel of Fig. 13 indicates a difference would be detectable at the $\geq 2\sigma$ ($p \leq 0.046$) level if the $SSFR_{H\alpha}$ deficits in the virialized region were increased by ~ 0.13 dex or more. Using boundary B2 instead shows that an even larger shift (0.18 dex or more) is required for a $\geq 2\sigma$ result. Thus, we rule out changes in $SSFR_{H\alpha}$ deficit across PPS diagram regions larger than 40–50 per cent.

5 DISCUSSION

5.1 Disentangling the effects of stellar mass and environment

Table 2 summarizes the significance of changes in the imaging-derived properties across PPS and stellar mass. An important point to note is that the galaxy properties considered here ($B - V$, Sérsic index, half-light radius, Hubble type and SED type) have trends with stellar mass that are much more significant ($p < 10^{-26}$) than

their trends across virialized and non-virialized PPS bins (columns 3–6). The effect of mass on these galaxy properties is far stronger than the environmental effects revealed by the PPS.

Columns 4 and 5 of Table 2 summarize the results of repeating the PPS analysis (Figs 7 and 9) for boundary B1 after binning by stellar mass. The significance of the p-values is reduced, in part because of the reduced sample sizes. However, as noted in Section 4.1, the variations of colour and SED type across the PPS at $M_\star > M_{50}$ are more significant (3.2σ and 2.3σ) than the change in stellar mass (0.90σ). The changes in colour and SED in the higher mass bin cannot be explained by stellar mass alone and must be a result of environment. To test to what extent mass differences within each bin could affect this conclusion, we have repeated the analysis using narrower mass bins (four bins instead of two, which is as far as we can go given the sample size). We are still able to detect environmentally driven colour changes at the $\sim 2.5\sigma$–3σ level in three out of the four bins, and the results are inconclusive in the other one. This new test supports the conclusions that environmentally driven colour changes are present at fix stellar mass.

Column 6 further shows the comparison using the alternate, more conservative PPS boundary B2. The p-values for boundary B2 are qualitatively similar to those for boundary B1, with the significance for changes in colour, Sérsic index and especially SED type being higher in column 6 due to the more conservative virialized region boundary. The disparity in colour (SED type) across all masses is 2.40σ (3.2σ) more significant than the change in stellar mass. Conducting the PPS analysis with boundary B2 after binning by stellar mass likewise yields results consistent with columns 4 and 5. That the same qualitative results are seen with the alternative PPS boundary indicates the phase-space analysis is robust to the choice of the virialized region boundary.

Table 2 shows that Sérsic index has a somewhat more significant, although still somewhat marginal, change across PPS than Hubble type. This may seem puzzling at first sight since Sérsic index usually correlates with Hubble type, albeit with large scatter. We must not forget that the visually determined Hubble type reflects multiple criteria, including bulge-to-disc ratio and the presence and tightness/smoothness of the spiral arms, while Sérsic index reflects
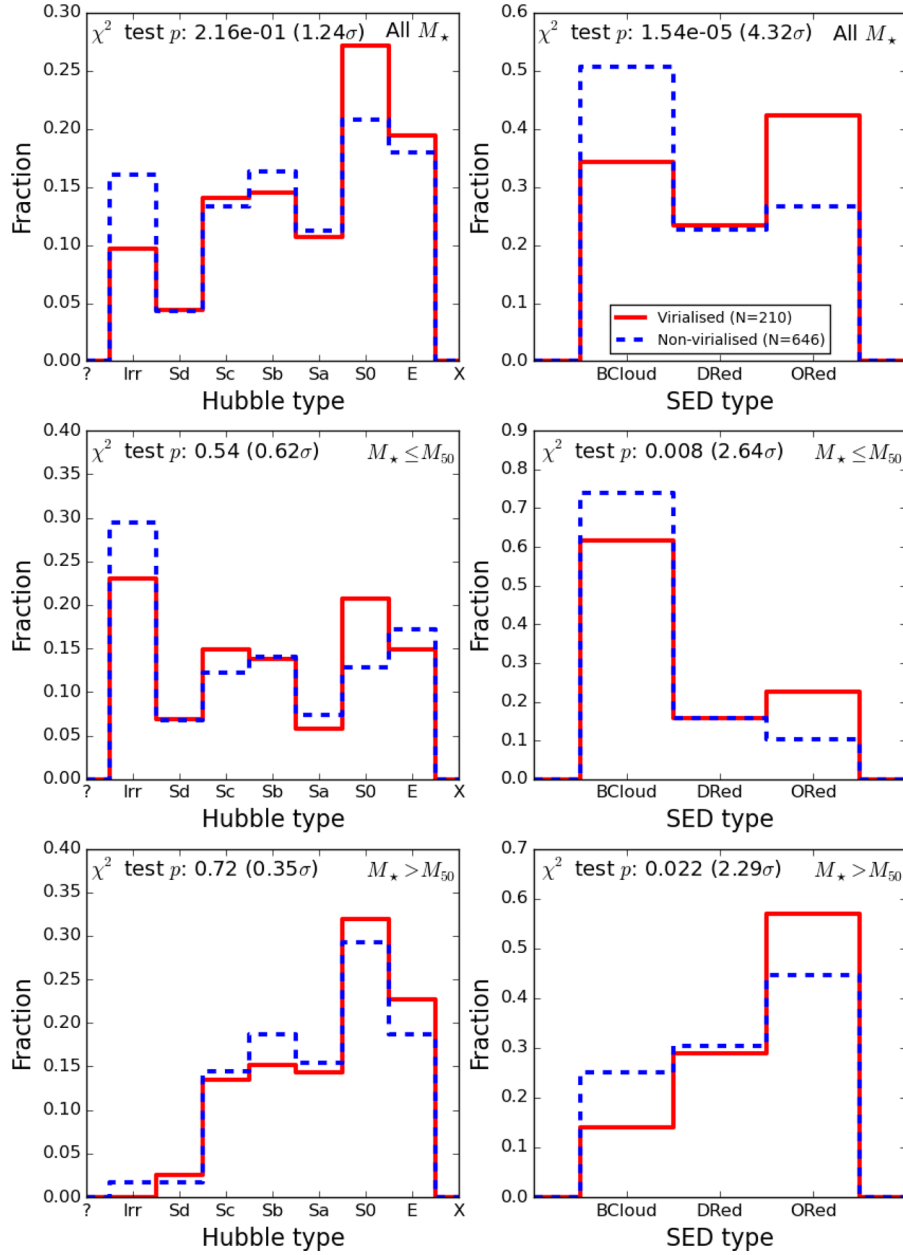
Figure 9. The disparity in morphology (left-hand column) and SED type (right-hand column) across the two phase-space bins. The top row makes the comparison using all stellar masses. The middle and bottom rows repeat the analysis for the lower mass bin ($M_\star \leq M_{50}$) and higher mass bin ($M_\star > M_{50}$), respectively. Like Fig. 7, the virialized region is defined using fiducial boundary B1.

only the relative dominance of the bulge or the disc component in a galaxy (e.g. Kormendy & Bender 2012). Since Sérsic index and morphology are not the same, finding differences in environmental behaviour should not be surprising. Furthermore, considering that the significance of the environmental differences detected in the Sérsic index distribution is small (always $<3\sigma$), and given the indirect connection between Sérsic index and visual morphology, this apparent discrepancy is not that surprising.

Thus, we find in A901/902 that colour appears to be changing independently of morphology and structure, with the 'Dusty Red' spirals being the prime examples of this effect in A901/902. This result is in agreement with previous studies concluding that the environment can drive changes in colour without changing morphology (e.g. Bamford et al. 2009; Skibba et al. 2009; Masters et al. 2010).

5.2 Properties of star-forming galaxies

We find multiple indications that the star formation properties of star-forming galaxies do not differ significantly across the PPS in A901/2. First, the proportion of $\geq 3\sigma$ star-forming galaxies (Section 4.2.1, Table 3) changes only at the $\sim 2.2\sigma$ level across the PPS, less significant than the change with stellar mass ($\sim 6.2\sigma$). Likewise, there is little evidence ($<2\sigma$) for changes in the [N II]/Hα metallicity (Section 4.2.2) and SSFR$_{H\alpha}$ deficit (Section 4.2.3).

Wolf et al. (2005, 2009) find 'Dusty Red' galaxies in A901/2 make up a significant fraction of the star-forming galaxies. These 'Dusty Red' galaxies constitute over half of star-forming galaxies at stellar masses in the range 10^{10}–10^{11} M$_\odot$, and they form stars ~ 4 times slower at fixed mass than blue galaxies in A901/2. The fact that many star-forming galaxies are red explains why rest-frame

Table 2. Changes in galaxy properties across stellar mass, PPS.

Property (1)	Method (2)	PPS, B1[a] (3)	PPS, B1[a] ($M_\star \leq M_{50}$) (4)	PPS, B1[a] ($M_\star > M_{50}$) (5)	PPS, B2[b] (6)
Stellar mass	KS test	1.07×10^{-3} (3.27σ)	3.73×10^{-2} (2.08σ)	3.66×10^{-1} (0.90σ)	1.17×10^{-2} (2.52σ)
Colour ($B - V$)	KS test	9.95×10^{-6} (4.42σ)	7.92×10^{-2} (1.76σ)	1.20×10^{-3} (3.24σ)	9.33×10^{-7} (4.91σ)
Sérsic index	KS test	1.09×10^{-2} (2.55σ)	4.98×10^{-2} (1.96σ)	3.23×10^{-1} (0.99σ)	4.71×10^{-3} (2.83σ)
Half-light radius	KS test	8.26×10^{-2} (1.74σ)	4.01×10^{-1} (0.84σ)	1.90×10^{-1} (1.31σ)	3.71×10^{-1} (0.89σ)
Hubble type	χ^2 test	2.16×10^{-1} (1.24σ)	5.38×10^{-1} (0.62σ)	7.25×10^{-1} (0.35σ)	3.14×10^{-2} (2.15σ)
SED type	χ^2 test	1.54×10^{-5} (4.32σ)	8.34×10^{-3} (2.64σ)	2.20×10^{-2} (2.29σ)	1.39×10^{-8} (5.67σ)

Notes. $M_{50} = 10^{9.85}$ M$_\odot$ is the 50th percentile in stellar mass.
[a]Tests the change in galaxy property inside and outside the virialized region in phase space defined by boundary B1, $R_p/R_{200} \leq 1.2$ and $|\Delta V_{los}/\sigma_{scl}| \leq 1.5 - 1.5/1.2 \times R_p/R_{200}$.
[b]Tests the change in galaxy property inside and outside a smaller virialized region in phase space defined by boundary B2, $R_p/R_{200} \leq 0.5$ and $|\Delta V_{los}/\sigma_{scl}| \leq 2.0 - 2.0/0.5 \times R_p/R_{200}$.
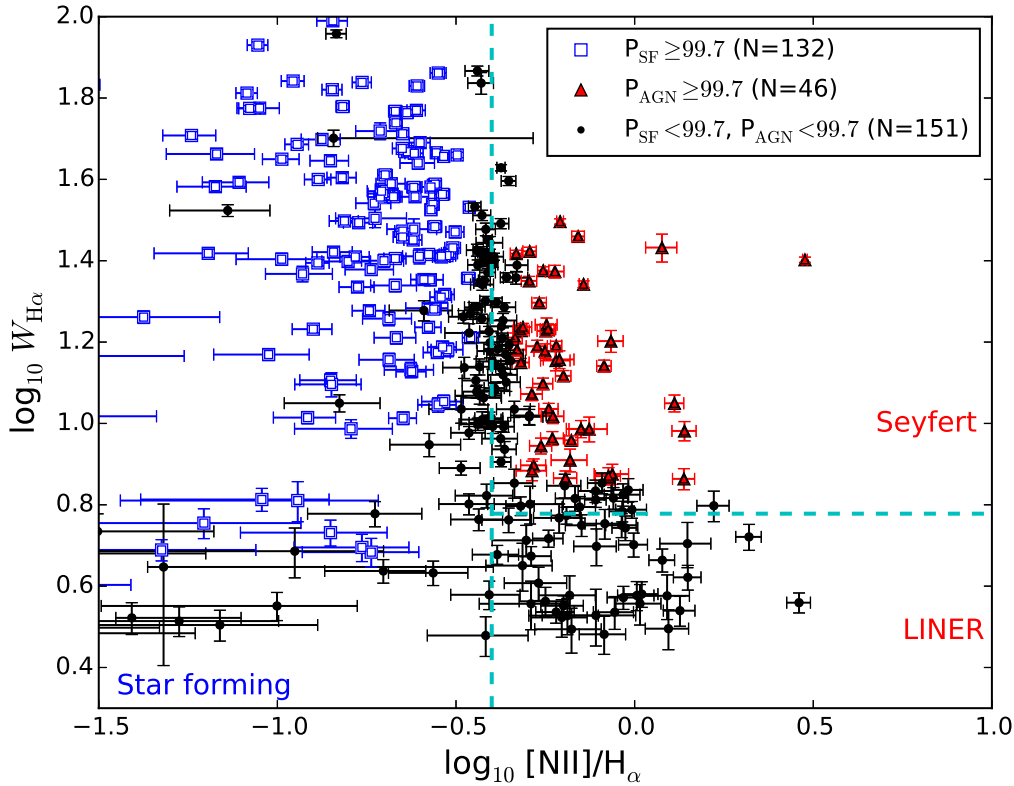

Figure 10. The WHAN diagram ([N II]/Hα gas-phase metallicity versus Hα equivalent width, $W_{H\alpha}$), introduced by Cid Fernandes et al. (2010, 2011), for the 329 OMEGA galaxies in sample S2 (Section 2.4) whose PSF-aperture spectra have both the Hα and [N II] lines within the wavelengths probed. Galaxies that are dominated by star formation or AGN activity at probability ≥99.7 per cent are distinguished. See Section 4.2.1 for details.

colours and SED types vary more strongly (Table 2) across the PPS than star formation properties.

Wolf et al. (2009) report an overall reduction in SSFR$_{UV + IR}$ of star-forming galaxies relative to the field, and a subtle change in SFR$_{UV + IR}$ across local density. Rodríguez del Pino et al. (2017) report at fixed mass a reduction in SSFR$_{H\alpha}$ of star-forming galaxies relative to the field. We see this offset too (Fig. 12), but we do not see a difference in SSFR$_{H\alpha}$ deficit within bins of the PPS (Fig. 13). A reduction in SSFR$_{H\alpha}$ relative to the field, but not across broad bins of the PPS, suggests the cluster galaxies are all being pre-processed (e.g. Zabludoff & Mulchaey 1998; Moran et al. 2007; Kautsch et al. 2008; Dressler et al. 2013; Haines et al. 2013; Cybulski et al. 2014; Lopes, Ribeiro & Rembold 2014) in a similar manner during infall, and much of the reduction in star formation activity has

already happened by the time the galaxies enter the broad cluster environment sampled by the OMEGA survey.

We find in Table 3 and Section 4.2.1 that the vast majority of star-forming galaxies are outside the virialized region (i.e. at large projected radius). The paucity of star-forming galaxies in the dense virialized region is consistent with studies of other galaxy clusters. Many authors have reported a star formation–density relation at $z \lesssim 1$ in which the fraction of star-forming galaxies declines from the cluster outskirts ($\sim R_{200}$) to the cluster core (Kodama et al. 2004; Finn et al. 2005; Rines et al. 2005; Koyama et al. 2010; Muzzin et al. 2012; Webb et al. 2013; Wegner, Chu & Hwang 2015). For example, Kodama et al. (2004) find that the fraction of galaxies detected in Hα strongly decreases with local density at $z = 0.4$. Finn et al. (2005) find no radial trend in star formation rates within

Table 3. Number of $\geq 3\sigma$ AGN and star-forming galaxies.

Condition	$\geq 3\sigma$ Star forming	$\geq 3\sigma$ AGN
Virialized region (B1[a])	27	17
Non-virialized region (B1[a])	105	29
Virialized region (B2[b])	7	7
Non-virialized region (B2[b])	125	39
$M_\star \leq M_{50}$[c]	108	15
$M_\star > M_{50}$[c]	24	31

Notes. [a]The virialized region in phase space is defined by boundary B1, $R_p/R_{200} \leq 1.2$ and $|\Delta V_{los}/\sigma_{scl}| \leq 1.5 - 1.5/1.2 \times R_p/R_{200}$.
[b]The virialized region in phase space is defined by boundary B2, $R_p/R_{200} \leq 0.5$ and $|\Delta V_{los}/\sigma_{scl}| \leq 2.0 - 2.0/0.5 \times R_p/R_{200}$.
[c]$M_{50} = 10^{9.85}$ M$_\odot$ is the 50th percentile in stellar mass.

three clusters at $z \sim 0.75$. They do find, however, that the fraction of star-forming galaxies increases (decreases) with projected distance (local density) in 2/3 clusters, which is consistent with our study.

Our results here showing rather small intracluster differences in star formation may, at first, seem to be in conflict with our

demonstration in Figs 7 and 8 of intracluster changes in galaxy colour. This is not a contradiction because these two results were obtained with different samples. The analysis on galaxy colour and other imaging properties involves all 856 galaxies in S2, whereas the analysis of Hα-based star formation properties was conducted with the significantly reduced subset of 351 *emission-line (primarily star-forming)* galaxies in S3 (Fig. 12). In other words, the environmental changes we have found in the colour distributions refer to the overall galaxy population, while any putative changes in star formation properties are only relevant to star-forming galaxies.

This is made explicit in Fig. 14, where we compare SSFR$_{H\alpha}$, $B - V$ and stellar mass for the smaller S3 sample of Hα-selected galaxies. The left column shows colour is very similar at both fixed SSFR$_{H\alpha}$ and mass. The right column shows the histograms of colour and SSFR$_{H\alpha}$ are not significantly different for the virialized and non-virialized Hα-emitting galaxies.

5.3 Properties of visually classified elliptical galaxies

It is well known that elliptical and early-type galaxies are relatively more abundant in dense environments than spiral galaxies (e.g.
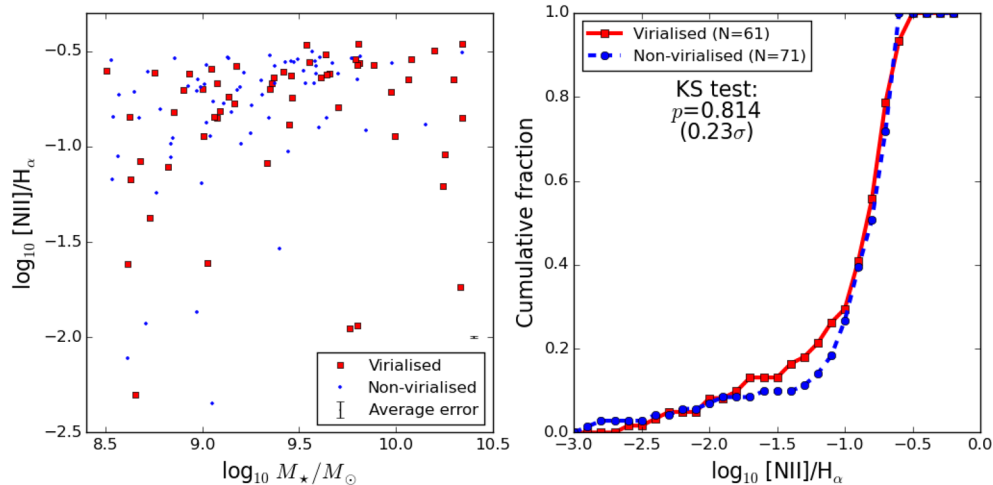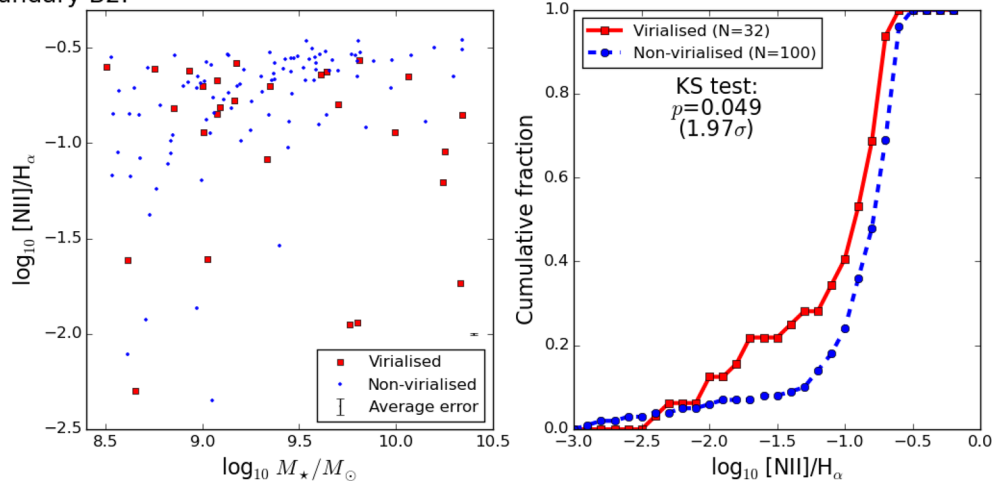

Figure 11. Potential change in gas-phase metallicity among the 132 galaxies whose PSF-aperture OMEGA spectra are dominated by star formation at the ≥ 99.7 per cent ($\geq 3\sigma$) level (see Section 4.2.1 for details). Top row: the left-hand panel shows the [N II]/Hα ratio versus stellar mass, colour coded by position in the PPS (with respect to the PPS boundary B1). The right-hand panel shows the corresponding cumulative distributions and results of a KS test. Bottom row: same as top row, except for the PPS boundary B2.
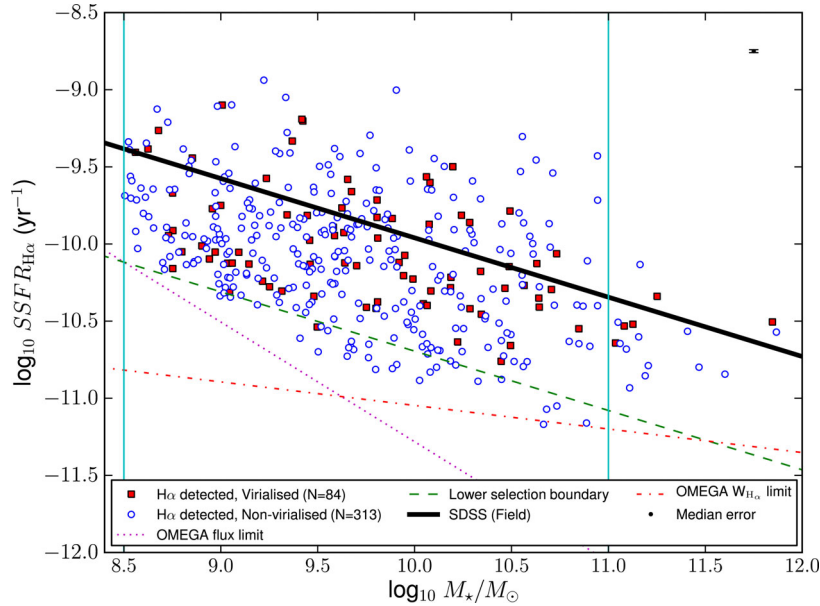
Figure 12. The SSFR$_{H\alpha}$–$M_\star$ relation (Section 4.2.3) is compared for the field and the 397 galaxies in sample S2 (Section 2.4) with large-aperture spectra from OMEGA (Section 2.3). The black line is the SSFR$_{H\alpha}$–$M_\star$ relation from SDSS (Abazajian et al. 2009). The dashed line is a boundary parallel to the SDSS relation that intersects the Hα flux limit (3×10^{-17} erg s^{-1} cm^{-2}) in OMEGA (dotted line). The dash–dotted line represents the 3 Å Hα equivalent width ($W_{H\alpha}$) detection limit. Sample S3 includes the 351 galaxies above the dashed line and between the vertical lines. The points are colour coded by galaxy position in the PPS, as defined by fiducial boundary B1. The error bar in the upper right corner shows the median error on SSFR$_{H\alpha}$. Also see Rodríguez del Pino et al. (2017) for a related diagram.
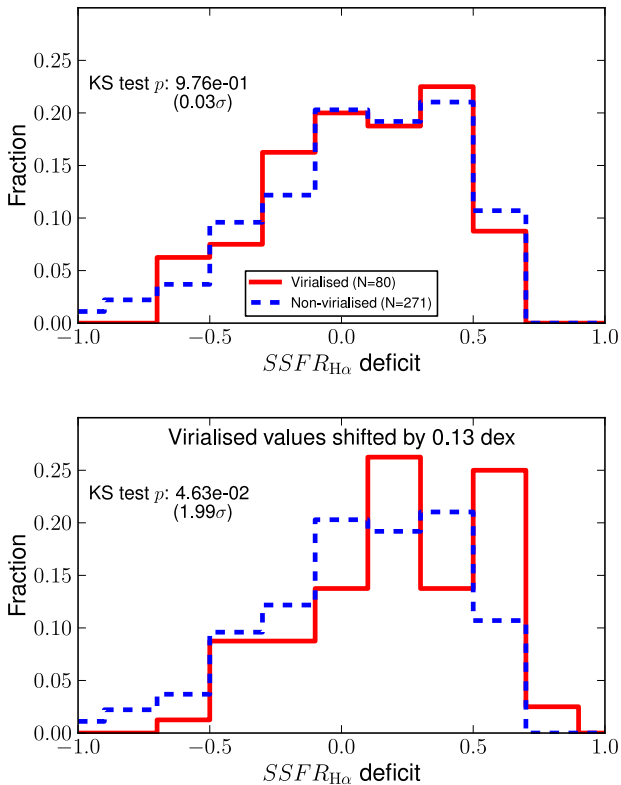

Figure 13. The top panel shows SSFR deficit histograms for sample S3 (Fig. 12) in the virialized and non-virialized regions (as defined by boundary B1). A KS test comparing SSFR deficit in the two PPS regions shows no significant difference ($p = 0.98$). The bottom panel indicates a distinction would be detectable at the $\geq 2\sigma$ level if the star formation deficits in the virialized region were increased by ~ 0.13 dex or more.

Dressler 1980; Postman & Geller 1984; Norberg et al. 2002; Goto et al. 2003; Blanton et al. 2005; Postman et al. 2005; Wolf et al. 2007; Ball et al. 2008). Fig. 7 and Table 2, though, show no variation in Hubble type across the PPS within A901/2. Furthermore, at fixed Hubble type (E, S0, Spirals Irr), we have checked for differences in galaxy stellar mass, rest frame colour and Sérsic index across the PPS. Visually classified elliptical galaxies are the only population showing marginally significant ($\sim 2\sigma$) changes in colour and stellar mass. No Hubble type shows a substantial change in Sérsic index across the PPS.

Fig. 15 shows the distributions of colour and stellar mass for the elliptical galaxies. The colour distributions of ellipticals are different between the PPS bins at the $>2\sigma$ level. This is true for either definition of the virialized region, although the difference is more significant for boundary B1 than B2 (2.9σ versus 2.0σ). The offset is driven by a population of infalling elliptical galaxies with $B - V < 0.7$ that is absent in the virialized region. The difference in stellar mass due to the PPS, by comparison, is weaker (1.9σ for B1 and 1.7σ for B2), indicating the change in colour cannot be explained only by the difference in stellar mass.

A possible caveat with the Hubble types used in this study is that some galaxies called 'elliptical' may not be true elliptical galaxies. Studies in the Virgo cluster show that most true elliptical galaxies are brighter than $M_V = -18$ (e.g. Kormendy et al. 2009). In our Fig. 8, however, most of the ellipticals with $B - V < 0.7$ are fainter than $M_V = -18$. Based on visual inspection, we are confident these objects are not dwarf irregulars. Many of them could instead be spheroidal galaxies, defunct late types transformed by environment (e.g. Kormendy et al. 2009; Kormendy & Bender 2012). The median Sérsic index ($n = 1.77$) of the blue ($B - V \leq 0.7$), visually classified ellipticals is compatible with this idea. The redder ($B - V > 0.7$) ellipticals, in comparison, have higher median Sérsic index ($n = 3.56$).
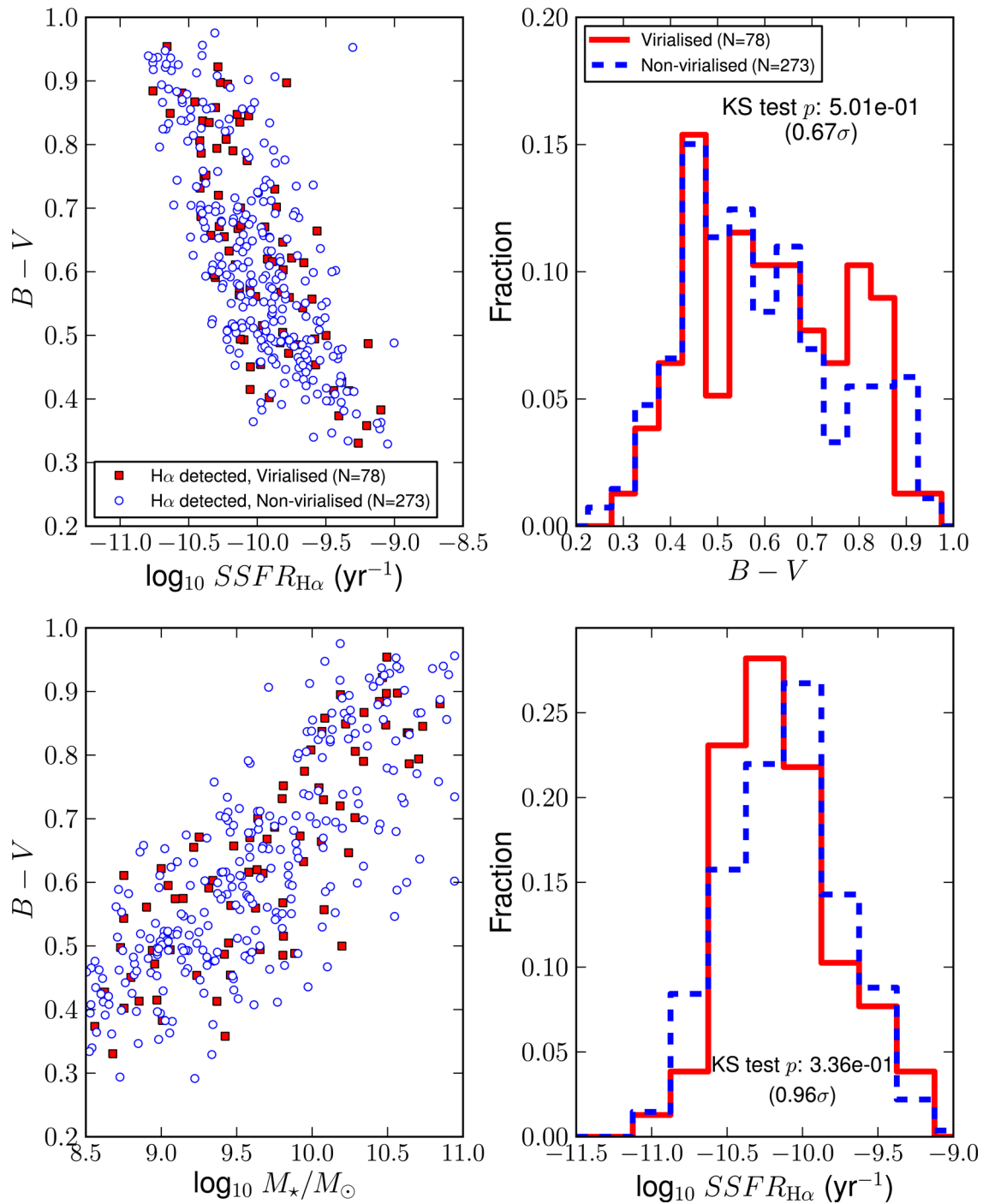
Figure 14. Comparison of SSFR$_{H\alpha}$, colour and stellar mass for the 351 Hα-emitting galaxies in sample S3 (defined in Fig. 12). The points are colour coded by galaxy position in the PPS, as defined by fiducial boundary B1.

5.4 Differences between the A901/2 subclusters

It is interesting to consider how galaxy properties differ across the PPS within the four A901/2 subclusters (Table 1). Table 4 summarizes the effect of the PPS on galaxy properties for each subcluster. Comparing Table 1 and Table 4 shows no correlation between subcluster halo properties and the contrast of galaxy properties across phase space. It is possible that spatial incompleteness (Fig. 5), especially for A902 and the SW Group, is a limiting factor in the comparison of individual subclusters.

For the PPS boundary B1, colour and SED type are the only properties consistently varying more strongly than stellar mass across the PPS in Table 4. Stellar mass changes by $>2\sigma$ only for the two more massive subclusters A901a and A901b. These two subclusters are apparently driving the stronger 3.3σ change found for stellar mass in Fig. 7 and Table 2. The individual subclusters show changes in colour at the 1.9σ–3.2σ level. Except for the SW Group, all subclusters show environmental changes in the SED type at the 2.2σ–2.8σ level.
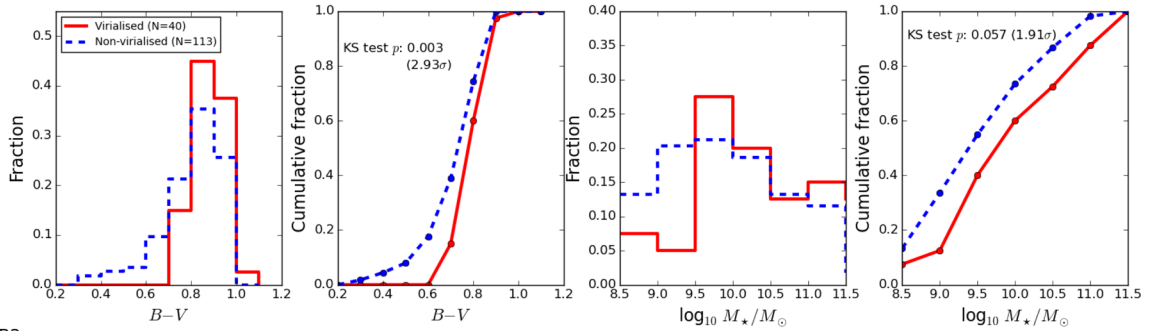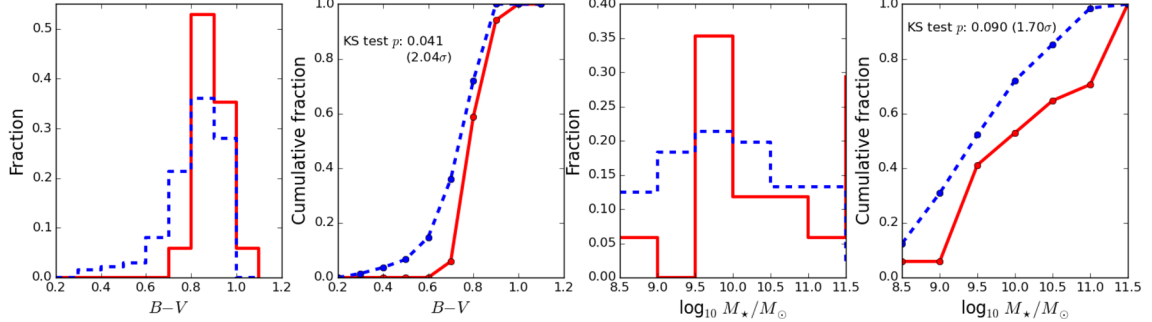
Figure 15. Exploring how stellar mass and rest-frame colour change for elliptical galaxies across the PPS. Top row: the distributions of rest-frame $B - V$ and stellar mass are shown for the two PPS bins (delineated by boundary B1), along with the corresponding cumulative distributions. Bottom row: the same, except the PPS bins are defined by boundary B2.

Table 4. Changes in galaxy properties across PPS and subcluster.

Cluster	Stellar mass	Colour ($B - V$)	Sérsic index	Half-light radius	Hubble type	SED type
			Boundary B1[a]			
A901a	3.28×10^{-2} (2.13σ)	1.59×10^{-2} (2.41σ)	1.98×10^{-2} (2.33σ)	1.09×10^{-1} (1.60σ)	1.13×10^{-1} (1.58σ)	2.65×10^{-2} (2.22σ)
A901b	2.01×10^{-2} (2.32σ)	1.37×10^{-3} (3.20σ)	7.18×10^{-2} (1.80σ)	4.98×10^{-1} (0.68σ)	8.18×10^{-3} (2.64σ)	4.54×10^{-3} (2.84σ)
A902	4.96×10^{-1} (0.68σ)	4.16×10^{-3} (2.87σ)	7.54×10^{-1} (0.31σ)	9.66×10^{-1} (0.04σ)	9.58×10^{-1} (0.05σ)	6.36×10^{-3} (2.73σ)
SW Group	2.08×10^{-1} (1.26σ)	6.50×10^{-2} (1.85σ)	2.59×10^{-1} (1.13σ)	1.30×10^{-1} (1.52σ)	1.20×10^{-1} (1.56σ)	4.10×10^{-1} (0.82σ)
			Boundary B2[b]			
A901a	7.70×10^{-2} (1.77σ)	3.12×10^{-3} (2.96σ)	2.78×10^{-1} (1.09σ)	4.22×10^{-1} (0.80σ)	5.25×10^{-1} (0.64σ)	2.99×10^{-5} (4.17σ)
A901b	2.40×10^{-1} (1.18σ)	3.00×10^{-2} (2.17σ)	4.89×10^{-2} (1.97σ)	8.79×10^{-1} (0.15σ)	2.92×10^{-1} (1.05σ)	9.07×10^{-3} (2.61σ)
A902	3.68×10^{-2} (2.09σ)	4.16×10^{-3} (2.87σ)	2.33×10^{-1} (1.19σ)	2.70×10^{-1} (1.10σ)	5.36×10^{-1} (0.62σ)	7.75×10^{-2} (1.77σ)
SW Group	5.89×10^{-1} (0.54σ)	1.02×10^{-1} (1.63σ)	2.45×10^{-2} (2.25σ)	5.89×10^{-1} (0.54σ)	2.18×10^{-1} (1.23σ)	8.94×10^{-2} (1.70σ)

Notes. [a]Tests the change in galaxy property inside and outside the virialized region in phase space defined by boundary B1, $R_p/R_{200} \leq 1.2$ and $|\Delta V_{los}/\sigma_{scl}| \leq 1.5 - 1.5/1.2 \times R_p/R_{200}$.
[b]Tests the change in galaxy property inside and outside a smaller virialized region in phase space defined by boundary B2, $R_p/R_{200} \leq 0.5$ and $|\Delta V_{los}/\sigma_{scl}| \leq 2.0 - 2.0/0.5 \times R_p/R_{200}$.

A similar contrast in galaxy properties across phase space is found for the more conservative PPS boundary B2. This again highlights the robustness of our conclusions to the particular choice of boundary for the virialized region. Colour changes in all subclusters more strongly than stellar mass. This is true for SED type in only 3/4 subclusters, with A902 being the exception.

6 SUMMARY

In this paper, we have conducted a comprehensive, *intracluster* analysis of the A901/2 multicluster system at $z \sim 0.165$. Aggregating redshifts from traditional spectroscopy, tunable-filter imaging and prism techniques, we have assembled redshifts for a sample of 856 cluster galaxies that reaches in stellar mass down to $10^{8.5}$ M$_\odot$.

This unique data set facilitates a more nuanced study of environment that goes beyond common field-versus-cluster comparisons. We have looked for variations in cluster galaxy properties between the virialized and non-virialized regions of projected phase space, using two different boundaries for the virialized region. Our main results, summarized below, highlight that A901/2 exhibits only relatively gentle environmental effects that act mainly on galaxy gas reservoirs.

(i) Stacking the four subclusters (Table 1) in A901/2 together, we find some significant changes across the PPS between the virialized and non-virialized regions for imaging-derived galaxy properties (Table 2 and Figs 7 and 9). With our fiducial definition of the virialized region (boundary B1), stellar mass, rest-frame $B - V$ colour

and SED type all differ between regions with $>3\sigma$ significance such that galaxies in the virialized region are more massive, have redder colours and have predominantly passive SED types. Additionally, Sérsic indices are larger, implying dynamically hotter stellar structures in the virialized region, at the 2.6σ level. Half-light radius and Hubble-type variations across the PPS are less significant. Similar results are found with a smaller, more conservative boundary (B2) for the virialized region.

(ii) Since stellar mass varies across phase space in conjunction with other galaxy properties, it is important to consider whether the apparent variation of these galaxy properties with phase space is just a mass effect. Indeed, KS test p-value significances for galaxy properties binned in stellar mass are tens of orders of magnitude stronger than the corresponding test statistics for galaxy properties binned just in PPS (Table 2, column 3).

(iii) The role of stellar mass is disentangled by conducting the PPS analysis in bins of stellar mass. At $M_\star > 10^{9.85}$ M$_\odot$, the 50th percentile in stellar mass, the change in rest-frame colour across the PPS is stronger (3.2σ versus 0.90σ) than the change in stellar mass across the PPS (Fig. 7 and Table 2). This is due to a population of relatively blue ($B - V < 0.7$) galaxies with mostly spiral Hubble types in the higher mass bin that exists in the non-virialized region but not the virialized region. The prominence of the colour disparity relative to the stellar mass change is even apparent in the individual subclusters (Table 4). This suggests the changes seen in rest-frame colour and SED type are driven to some degree by environmental processes.

(iv) While Hubble type does not change significantly across the PPS, visually classified elliptical galaxies as a group are slightly bluer with $\sim2\sigma$ significance in the non-virialized region (Fig. 15). This is due to an infalling population of lower mass ($M_\star \leq 10^{9.85}$ M$_\odot$) ellipticals with $B - V < 0.7$ that is absent in the virialized region. It is important to note that some of the low-luminosity ($M_V > -18$), blue ($B - V < 0.7$) galaxies responsible for this result could be spheroidal galaxies rather than true ellipticals.

(v) The proportions of bona fide star-forming and AGN galaxies change much less in the PPS than with stellar mass. Still, there is a reduction in the frequency of star-forming galaxies in the virialized region (Table 3) that is consistent with the star formation–density relation observed in other clusters.

(vi) The [N II]/Hα metallicity and SSFR$_{H\alpha}$ deficit differ at $<2\sigma$ significance across the PPS. We do, however, see at fixed mass an overall reduction in SSFR$_{H\alpha}$ relative to the field (Fig. 12), a result found in parallel by Rodríguez del Pino et al. (2017). These observations suggest that pre-processing of galaxies during infall plays a prominent role in quenching star formation.

Our study of galaxy properties across projected phase space in A901/2 provides compelling evidence for the action of environmental processes. Since the strongest observable changes in galaxy properties pertain to colour and SED type, the environmental processes must be gentle and manifest primarily on the gas reservoirs rather than the underlying stellar structures. Similar conclusions have been reached for A901/2 previously by Bösch et al. (2013) and Maltby et al. (2015) and most recently by Rodríguez del Pino et al. (2017) through a complementary analysis.

Additional progress in disentangling galaxy environment effects is possible with spatially resolved measures of star formation and kinematics from integral field units. This will allow a study in which the spatial distributions and kinematics of young/old stars and ionized gas can be compared consistently for galaxies spanning a wide range of environment, stellar mass, star formation and morphology. Studies of this nature are already possible with data from the Sydney-AAO Multi-Object Integral Field Spectrograph (SAMI; Croom et al. 2012) and Mapping Nearby Galaxies at Apache Point Observatory (MaNGA; Bundy et al. 2015) galaxy surveys.

REFERENCES

Abazajian K. N. et al., 2009, ApJS, 182, 543
Andredakis Y. C., Peletier R. F., Balcells M., 1995, MNRAS, 275, 874
Ball N. M., Loveday J., Brunner R. J., 2008, MNRAS, 383, 907
Bamford S. P. et al., 2009, MNRAS, 393, 1324
Barnes J. E., 1988, ApJ, 331, 699
Barnes J. E., Hernquist L. E., 1991, ApJ, 370, L65
Bauer A. E., Grützbauch R., Jørgensen I., Varela J., Bergmann M., 2011, MNRAS, 411, 2009
Beers T. C., Flynn K., Gebhardt K., 1990, AJ, 100, 32
Bell E. F. et al., 2004, ApJ, 608, 752
Bell E. F., Zheng X. Z., Papovich C., Borch A., Wolf C., Meisenheimer K., 2007, ApJ, 663, 834
Birnboim Y., Dekel A., 2003, MNRAS, 345, 349
Blanton M. R., Eisenstein D., Hogg D. W., Schlegel D. J., Brinkmann J., 2005, ApJ, 629, 143
Borch A. et al., 2006, A&A, 453, 869
Bösch B. et al., 2013, A&A, 549, A142
Brinchmann J., Charlot S., White S. D. M., Tremonti C., Kauffmann G., Heckman T., Brinkmann J., 2004, MNRAS, 351, 1151
Bundy K. et al., 2015, ApJ, 798, 7
Butcher H., Oemler A., Jr, 1984, ApJ, 285, 426
Cepa J., 2013, Rev. Mex. Astron. Astrofis. Conf. Ser., 42, 77
Cid Fernandes R., Stasińska G., Mateus A., Vale Asari N., 2011, MNRAS, 413, 1687
Cid Fernandes R., Stasińska G., Schlickmann M. S., Mateus A., Vale Asari N., Schoenell W., Sodré L., 2010, MNRAS, 403, 1036
Chies-Santos A. L. et al., 2015, MNRAS, 450, 4458
Coil A. L. et al., 2011, ApJ, 741, 8
Cooper M. C. et al., 2007, MNRAS, 376, 1445
Cooper M. C. et al., 2008, MNRAS, 383, 1058
Croom S. M. et al., 2012, MNRAS, 421, 872
Cybulski R., Yun M. S., Fazio G. G., Gutermuth R. A., 2014, MNRAS, 439, 3564
de Jong R. S., 1996, A&AS, 118, 557
Dekel A., Birnboim Y., 2006, MNRAS, 368, 2
Denicoló G., Terlevich R., Terlevich E., 2002, MNRAS, 330, 69
Desai V. et al., 2007, ApJ, 660, 1151
Diaferio A., Geller M. J., 1997, ApJ, 481, 633
Dressler A., 1980, ApJ, 236, 351
Dressler A., Oemler A., Jr, Poggianti B. M., Gladders M. D., Abramson L., Vulcani B., 2013, ApJ, 770, 62
Finn R. A. et al., 2005, ApJ, 630, 206
Fujita Y., Nagashima M., 1999, ApJ, 516, 619

Gilmour R., Gray M. E., Almaini O., Best P., Wolf C., Meisenheimer K., Papovich C., Bell E., 2007, MNRAS, 380, 1467

Gnedin O. Y., 2003, ApJ, 589, 752

Goto T., Yamauchi C., Fujita Y., Okamura S., Sekiguchi M., Smail I., Bernardi M., Gomez P. L., 2003, MNRAS, 346, 601

Graham A. W., Guzmán R., 2003, AJ, 125, 2936

Gray M. E. et al., 2002, ApJ, 568, 141

Gray M. E. et al., 2009, MNRAS, 393, 1275

Gunn J. E., Gott J. R., III, 1972, ApJ, 176, 1

Haines C. P. et al., 2013, ApJ, 775, 126

Hashimoto Y., Oemler A., Jr, Lin H., Tucker D. L., 1998, ApJ, 499, 589

Hernández-Fernández J. D., Haines C. P., Diaferio A., Iglesias-Páramo J., Mendes de Oliveira C., Vilchez J. M., 2014, MNRAS, 438, 2186

Heymans C. et al., 2008, MNRAS, 385, 1431

Hilz M., Naab T., Ostriker J. P., 2013, MNRAS, 429, 2924

Hopkins P. F., Cox T. J., Younger J. D., Hernquist L., 2009, ApJ, 691, 1168

Jaffé Y. L., Smith R., Candlish G. N., Poggianti B. M., Sheen Y.-K., Verheijen M. A. W., 2015, MNRAS, 448, 1715

Jogee S., Scoville N., Kenney J. D. P., 2005, ApJ, 630, 837

Kautsch S. J., Gonzalez A. H., Soto C. A., Tran K.-V. H., Zaritsky D., Moustakas J., 2008, ApJ, 688, L5

Kennicutt R. C., Jr, 1998, ARA&A, 36, 189

Kereš D., Katz N., Weinberg D. H., Davé R., 2005, MNRAS, 363, 2

Khochfar S., Silk J., 2006, MNRAS, 370, 902

Khochfar S., Silk J., 2009, MNRAS, 397, 506

Khosroshahi H. G., Wadadekar Y., Kembhavi A., 2000, ApJ, 533, 162

Kodama T., Balogh M. L., Smail I., Bower R. G., Nakata F., 2004, MNRAS, 354, 1103

Kormendy J., 1993, in DeJonghe H., Habing H. J., eds, Proc. IAU Symp. 153, Galactic Bulges. Kluwer, Dordrecht, p. 209

Kormendy J., Bender R., 2012, ApJS, 198, 2

Kormendy J., Kennicutt R. C., Jr, 2004, ARA&A, 42, 603

Kormendy J., Fisher D. B., Cornell M. E., Bender R., 2009, ApJS, 182, 216

Koyama Y., Kodama T., Shimasaku K., Hayashi M., Okamura S., Tanaka I., Tokoku C., 2010, MNRAS, 403, 1611

Lange R. et al., 2015, MNRAS, 447, 2603

Larson R. B., Tinsley B. M., Caldwell C. N., 1980, ApJ, 237, 692

Lidman C. et al., 2008, A&A, 489, 981

Lopes P. A. A., Ribeiro A. L. B., Rembold S. B., 2014, MNRAS, 437, 2430

Mahajan S., Mamon G. A., Raychaudhury S., 2011, MNRAS, 416, 2882

Maltby D. T. et al., 2010, MNRAS, 402, 282

Maltby D. T., Aragón-Salamanca A., Gray M. E., Hoyos C., Wolf C., Jogee S., Böhm A., 2015, MNRAS, 447, 1506

Masters K. L. et al., 2010, MNRAS, 405, 783

Moore B., Katz N., Lake G., Dressler A., Oemler A., 1996, Nature, 379, 613

Moran S. M., Ellis R. S., Treu T., Smith G. P., Rich R. M., Smail I., 2007, ApJ, 671, 1503

Muzzin A. et al., 2012, ApJ, 746, 188

Muzzin A. et al., 2014, ApJ, 796, 65

Nagao T., Maiolino R., Marconi A., 2006, A&A, 459, 85

Noble A. G., Webb T. M. A., Yee H. K. C., Muzzin A., Wilson G., van der Burg R. F. J., Balogh M. L., Shupe D. L., 2016, ApJ, 816, 48

Norberg P. et al., 2002, MNRAS, 332, 827

Ocvirk P., Pichon C., Teyssier R., 2008, MNRAS, 390, 1326

Oman K. A., Hudson M. J., Behroozi P. S., 2013, MNRAS, 431, 2307

Oser L., Naab T., Ostriker J. P., Johansson P. H., 2012, ApJ, 744, 63

Patel S. G., Holden B. P., Kelson D. D., Illingworth G. D., Franx M., 2009, ApJ, 705, L67

Pettini M., Pagel B. E. J., 2004, MNRAS, 348, L59

Poggianti B. M. et al., 2001, ApJ, 563, 118

Poggianti B. M. et al., 2008, ApJ, 684, 888

Postman M., Geller M. J., 1984, ApJ, 281, 95

Postman M. et al., 2005, ApJ, 623, 721

Regos E., Geller M. J., 1989, AJ, 98, 755

Rines K., Geller M. J., Kurtz M. J., Diaferio A., 2005, AJ, 130, 1482

Rodríguez del Pino B. et al., 2017, MNRAS, 467, 4200

Sérsic J. L., 1963, Bol. Asociacion Argentina Astron., 6, 41

Skibba R. A. et al., 2009, MNRAS, 399, 966

Taranu D. S., Hudson M. J., Balogh M. L., Smith R. J., Power C., Oman K. A., Krane B., 2014, MNRAS, 440, 1934

Toomre A., 1977, in Tinsley B. M., Larson R. B. G., Campbell D., eds, Evolution of Galaxies and Stellar Populations. Yale Univ. Observatory, New Haven, p. 401

Tran K.-V. H., van Dokkum P., Illingworth G. D., Kelson D., Gonzalez A., Franx M., 2005, ApJ, 619, 134

Webb T. M. A. et al., 2013, AJ, 146, 84

Wegner G. A., Chu D. S., Hwang H. S., 2015, MNRAS, 447, 1126

Weinzirl T. et al., 2011, ApJ, 743, 87

Weinzirl T. et al., 2014, MNRAS, 441, 3083

Weinzirl T., Aragón-Salamanca A., Bamford S. P., Rodríguez del Pino B., Gray M. E., Chies-Santos A. L., 2015, MNRAS, 454, 1387

Wolf C., Meisenheimer K., Rix H.-W., Borch A., Dye S., Kleinheinrich M., 2003, A&A, 401, 73

Wolf C., Gray M. E., Meisenheimer K., 2005, A&A, 443, 435

Wolf C., Gray M. E., Aragón-Salamanca A., Lane K. P., Meisenheimer K., 2007, MNRAS, 376, L1

Wolf C. et al., 2009, MNRAS, 393, 1302

Zabludoff A. I., Mulchaey J. S., 1998, ApJ, 496, 39

This paper has been typeset from a TeX/LaTeX file prepared by the author.